EXPERIMENTAL STUDY ON THE STRENGTH OF TL-5 CONCRETE BRIDGE BARRIER REINFORCED WITH STAINLESS STEEL BARS

By

Alexander Ruta

B.Eng., Ryerson University, Canada, 2017

An MRP
presented to Ryerson University

in partial fulfillment of the
requirements for the degree of
Master of Engineering
in the program of
Civil Engineering

Toronto, Ontario, Canada, 2020

Author's Declaration

I hereby declare that I am the sole author of this MRP. This is a true copy of the MRP, including any required final revisions.

I authorize Ryerson University to lend this MRP to other institutions or individuals for the purpose of scholarly research.

I further authorize Ryerson University to reproduce this MRP by photocopying or by other means, in total or in part, at the request of other institutions or individuals for the purpose of scholarly research.

I understand that my MRP may be made electronically available to the public.

Abstract

EXPERIMENTAL STUDY ON THE STRENGTH OF TL-5 CONCRETE BRIDGE BARRIER REINFORCED WITH STAINLESS STEEL BARS

By

Alexander Ruta

Master of Engineering

Civil Engineering, Ryerson University

Toronto, Ontario, Canada

2020

AASHTO-LRFD Bridge Design Specifications provide equations for the flexural capacity of concrete barriers subjected to vehicle impact based on the yield-line theory. However, no experimental testing nor computer modelling was found in the literature to support the AASHTO-LRFD triangular yield-line failure pattern. The objective of this study is to generate experimental research data on the behavior of Test-Level 5 (TL-5) concrete barrier reinforced with stainless steel bars when subjected to transverse vehicular loading. The experimental program included testing four actual-size barriers, two of 6.5 m length and two of 4.5 m length. One barrier in each group was cast over a thick undeformable concrete base, while the other barrier was cast over a short slab cantilever. The 6.5 m long barriers were tested under a transverse line load centered at their mid-length, while the 4.5 m long barriers were tested under transverse exterior line loading. Results showed a trapezoidal flexural crack pattern in the barrier wall in contrast to the AASHTO-LRFD triangular yield-line pattern. The 4.5 m long barrier supported on thick concrete slab and the two 6.5 m long barriers failed in a punching shear mode. While the 4.5 m long barrier supported on a cantilever failed due to flexural cracks in the barrier wall and the slab cantilever along with anchorage cracks at the bottom end of the diagonal bent bars in the barrier wall embedded in the deck slab. Finally, the experimental transverse capacity of the tested barriers was greater than the design value in the Canadian Highway Bridge Design Code. However, it is recommended to increase the embedment length of the diagonal bent bars at the barrier-deck junction to be 185 mm instead of 125 mm to assist in altering the observed flexural/anchorage failure mode to punching shear failure at greater applied loading.

Acknowledgements

The author would like to express his gratitude sincerely to his supervisor Dr. Khaled Sennah for giving this amazing research opportunity. This study could not have been accomplished without his continuous guidance, suggestions and encouragements. I would also like to thank the laboratory technical staff Nidal Jaalouk, Khaleel Stoney, Bilal Baradie and Dominic Valle for their assistance in performing the experimental tests and for their continuous support throughout the entire research project. I would like to thank former undergraduate students Ahmed Elsayed, Monish Lad, Vansh Dave, and Mayssa Jeridi for their assistance in building the barrier specimens.

Dedication

TO MY FAMILY

for always loving and supporting me through each venture in my life

Table of Contents

List of Tables

List of Figures

Abbreviations

AASHTO	American Association of State Highway and Transportation Officials
ACI	American Concrete Institute
CDR	Capacity-Demand Ratio
CHBDC	Canadian Highway Bridge Design Code
COV	Coefficient of Variation
CSA	Canadian Standards Association
GFRP	Glass Fiber Reinforced Polymer
LRFD	Load Resistance Factor Design
LVDT	Linear Variable Displacement Transducer
MASH.	Manual for Assessing Safety Hardware
MTO	The Ministry of Transportation of Ontario
NCHRP	National Cooperative Highway Research Program
TL	Test Load

List of Symbols

C_E	Environmental coefficient
$b_{o,0.5d}$	Critical perimeter measured at a distance 0.5d to the loading patch area
d	Effective depth of concrete section
f'_c	28-day concrete compressive strength
F_t	Impact load
H	Height of barrier wall
K_1	Variable enhancement factor for support compression
L_c	Critical length
L_t	Length of transverse line load
M_b	Flexural resistance of cap beam (if applicable)
$M_{c,\ base}$	Flexural resistance of barrier about its horizontal axis at the base
$M_{c,\ w}$	Flexural resistance of barrier about its horizontal axis at the wall
M_w	Flexural resistance of barrier about its vertical axis
n	Number of samples
R_w	Transverse impact load resistance
V	Coefficient of variation
V_c	Punching shear capacity
w_t	Total external work due to applied load
X	Length of horizontal yield line
α	Yield line angle; refer to Figure 2. 7
α_s	Factor to adjust Vc for support dimensions
β	Yield line angle; refer to Figure 2. 7
β_c	Ratio of the long side to short side of the concentrated load or loading patch
γ_b	Partial safety factor to account for concrete compressive strengths
γ_m	Partial factor of safety
δ	Transverse displacement of wall due to applied load
θ	Yield line angle; refer to Figure 2. 7
λ	Concrete density
μ	Mean value

ρ	Reinforcement ratio
σ	Standard deviation
φ_c	Concrete resistance factor

Chapter I

Introduction

1.1 General

Bridge barriers and bridge barrier designed to date were required to meet the requirement for crash and safety in accordance with National Cooperative Highway Research Program (NCHRP) Report 350 "*Recommended Procedures for the Safety Performance Evaluation of Highway Features*" (Ross et al., 1993). The design forces for bridge barriers specified in Canadian Highway Bridge Design Code, CHBDC, (CSA, 2019) is based on AASHTO-LRFD Guide Specification for Bridge Rails (AASHTO, 1989) that corresponds to the test levels stipulated in NCHRP Report 350. Accordingly, CHBDC requires that appropriateness of bridge barrier anchorage system to the deck should be based on its performance during crash testing of the traffic barriers. Crash testing of a bridge barrier is carried out to investigate suitability of traffic barriers against structural adequacy, occupant risk and vehicle trajectory after the collision. The purpose of the concrete traffic barriers is to redirect an errant vehicle in a controlled manner in the event of a collision. The vehicle shall not penetrate, over-turn or roll-over the impacted traffic barriers. It should also not cause a secondary accident with the vehicles in other lanes. In addition, traffic barriers should have sufficient strengths to endure primary impact caused by the collision and remain effective in redirecting of vehicles after the impact. CHDBC also specifies if crash testing of traffic barriers is not available, the suitability of traffic barrier-deck anchorage shall be investigated based on the static test-to-complete collapse of the traffic barriers or approved numerical method of analysis and design. However, the ultimate strength of traffic barriers tested under static load should be greater than the maximum transverse load limits specified in CHDBD, that is 357 kN and 170 kN for Test-Level 5 (TL-5) and Test-Level 4 (TL-4) traffic barriers, respectively. The corresponding values in AASHTO-LRFD are 550 kN (124 kips) and 240 kN (54 kips) for Test Level 5 (TL-5) and (TL-4), respectively.

The following sections cover the need to carry out this research, the objectives and scope, and an overview of the entire report.

1.2 The Dilemma and Need for the Research

AASHTO-LRFD Bridge Design Specifications (AASHTO, 2017) specify equations for the flexural capacity of concrete barriers subjected to vehicle impact based on the yield-line theory. However, no experimental testing nor computer modelling was found in the literature to support the AASHTO-LRFD triangular yield-line failure pattern. Most recently, few authors proposed another yield line pattern to determine the barrier transverse flexural capacity in the form of trapezoidal yield line shape. Others considered punching shear failure of the barrier wall under vehicle impact. As such, experimental research data on the behavior of such barrier walls under transverse vehicular loading is needed. Ontario Ministry of Transportation (MTO) provides engineers and consultants with standard drawings for stainless steel bridge barrier for sustainable bridge construction. Bridge barriers constructed using regular steel reinforcement are prone to corrosion attack due to de-icing salt. In turn, constant maintenance and repair is required throughout the barriers life-cycle to combat the damage from corrosion. The use of stainless-steel reinforcement in future concrete barrier walls will eliminate the problem of corrosion hence significantly lowering the costs for maintenance and repair. Since no experimental testing was conducted in a stainless-steel reinforced bridge barrier, the current research is proposed.

1.3 Research Objectives

Static load tests on four full-scale TL-5 bridge barriers constructed with stainless-steel reinforcement were performed for the following objectives:

(i) Verify the stainless steel-reinforced barrier adequacy to resist the equivalent transverse static load simulating vehicle collision specified in CHBDC.

(ii) Examine the flexural crack pattern with respect to being triangular or trapezoidal in shape and the associated failure mode whether being due to flexure or punching shear.

(iii) Provide experimental data that can be used further in verifying computer modelling in future research.

1.4 Scope of the Research

A total of four full-scale TL-5 specified barrier walls were constructed using stainless-steel reinforcement.

(i) Specimen S-1: the barrier was of 4.5 m length supported over a thick nondeformable concrete base to simulate impact loading at barrier end (expansion joint).

(ii) Specimen S-2: the barrier was of 4.5 m length supported over a deck slab cantilever to simulate impact loading at barrier end.

(iii) Specimen S-3: the barrier was of 6.5 m length with a thick nondeformable concrete base to simulate vehicle impact loading within the barrier.

(iv) Specimen S-4: the barrier was of 6.5 m length built integrally on a cantilever deck slab to simulate vehicle impact loading within the barrier.

The thick concrete base used in specimens S-1 and S-3 represents the case of bridge barrier mounted over thick deck superstructure that is considered non-deformable compared to the size of the mounted barrier wall such as the cases of thick solid slab and voided slab bridges and the composite shear-connected box beam bridges. The static load was applied as a line load over 2.4 m length of the barrier wall as shown in Figure 1.1. The load was applied in increments to allow time to observe crack initiation and propagation. The experimental ultimate load was compared to the CHBDC design values. Discussion on the research findings was presented, followed by conclusions and recommendations for future research.

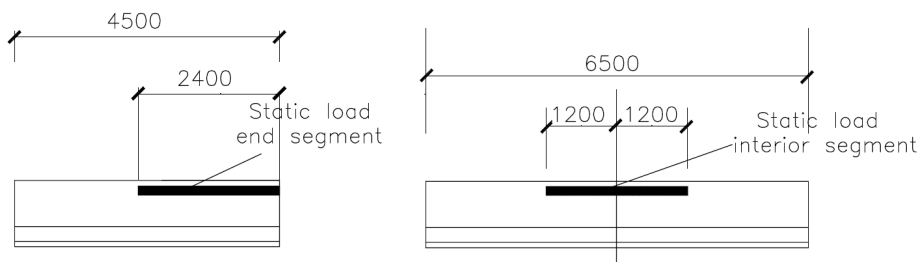

(a) Barrier S-1 and S-2 loaded at end location

(b) Barriers S-3 and S-4 loaded at interior location

Figure 1.1 Visual schematics of barrier length and load location for the four TL-5 specimens

1.5 Significance of the Research

The current market in Ontario for bridge barrier construction is primarily dominated by the use of glass fibre reinforced polymer (GFRP) bars and stainless-steel bars. This research will provide research information on the performance of stainless steel in bridge barriers subjected to transverse vehicular loading. Also, it provides experimental data on the failure modes of such barrier type when impacted by vehicle at interior and end segments.

1.6 Content and Arrangement of the Thesis

Chapter II on the literature review discusses relative background material related to this research such as the development of yield line equations for barrier wall failure and crash tests involving barrier walls with different reinforcement materials. Chapter III outlines in detail the entire experimental program. Chapter IV covers the discussion of the experimental results. Chapter V summarizes the conclusions and recommendations for future research.

Chapter II

Literature Review

2.1 General

This literature review Chapter covers relevant background material for the current research. It includes a summary of barrier geometries, design loads, crash testing, yield-line theory, punching shear capacities, and repair methods of existing barriers.

2.2 Barrier Types, Geometry and Design Loads

2.2.1 Barrier Types

As per CHBDC, barrier types are organized into a few major categories, namely: traffic, pedestrian, bicycle, a combination between traffic and pedestrian use, and a combination between traffic and bicycle use. Traffic barriers are classified as TL-1, TL-2, TL-4, and TL-5 based on their ability to withstand the highest vehicular impact load for low-, medium- and heavy-traffic roadways. The below table summarizes each barrier type with its corresponding design height in accordance with CHBDC.

Type of barrier	*H*, m
Traffic	
TL-1	0.68
TL-2	0.68
TL-4	0.80
TL-5	1.05†
Combination (pedestrian)	1.05
Combination (bicycle)	1.37
Pedestrian	1.05
Bicycle	1.37

**The height of the barrier is the vertical distance from the top to the bottom of the roadway, sidewalk, or bikeway face of the barrier, as applicable. For combination barriers, the height of the barrier is measured on the sidewalk or bikeway face of the barrier.*
†For freeways and high-speed rural arterial highways, consideration shall be given to increasing the barrier height to 1.37 m.

Figure 2.1 Vertical design heights correspomnding to the various barrier types (CSA Group, 2014)

2.2.2 Barrier Geometry

GM Shape

The original barrier shape was developed by General Motors (GM) and is called the GM shape. This barrier type incorporates a shallow lower slope and a steep upper slope. The shallow slope is beneficial for low angle impacts and allows the vehicle to be redirected with little damage. Consequently, the steep slope redirects vehicles with high angle impacts.

New Jersey Shape

The New Jersey shape barrier has essentially the same geometrical properties as the GM shape, the difference being a decrease in the shallow slope length and an increase in the steep slope length. The New Jersey shape also introduced a taller version of the barrier which accommodates larger vehicle impacts such as tractor trailers. Overall the increase in climb on the barrier helps reduce the impact force on the vehicle, however higher vehicle speeds introduces large vehicular roll angles leading to a vehicle role over after the collision.

The F-Shape

The F-Shape barrier was then designed to help resolve the issues of large vehicle climb and rollover (Rosenbaugh et al., 2007). The shallow slope was decreased in length and the steep slope was increased in length. It was found that so far this shape yielded the lowest vehicle climb and roll, however the maximum impact angle studied was only 15°.

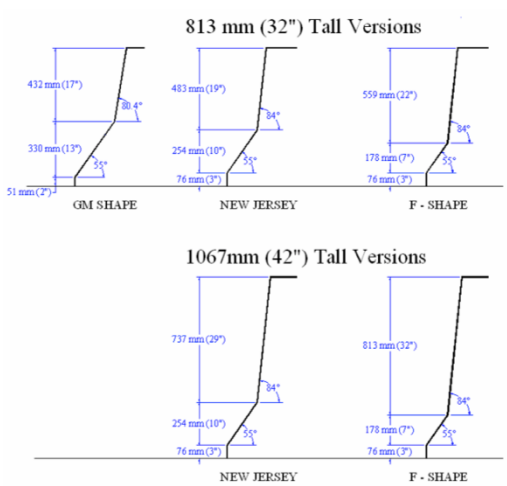

Figure 2.2 Evolution of multi-sloped barrier faces
(Rosenbaugh et al., 2007)

Constant Slope Barrier

The constant slope barrier is introduced by eliminating the lower slope found on the previous barrier shapes. Vehicle stability is greatly increased even with increased impact angles. However, having only one slope limits vehicular movement leading to a shorter impact duration. This shorter duration causes higher peak impact forces. Within the constant slope barrier shape, the completely vertical face serves as the most critical slope. The vertical face significantly limits lateral vehicle movement so there is only a horizontal component to the impact force. As a result, the vehicle will experience the highest impact force if the barrier face is completely vertical. Two prominent constant slope barriers found in the literature are the Texas SSCB and the California Type 60.

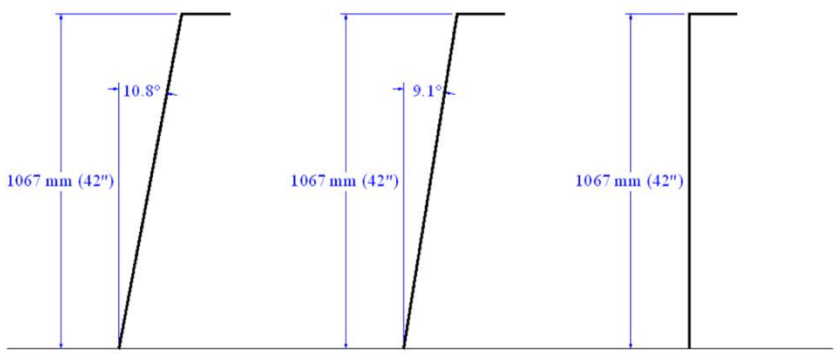

Figure 2.3 Popular industry standard constant-sloped barriers
(Rosenbaugh et al., 2007)

2.2.3 Barrier Design Loads

Applied forces used in today's bridge barrier design are specified in AASHTO-LRFD Bridge Design Specifications for TL-1 through TL6 barrier shapes as well as CHBDC for only TL-1, TL-2, TL-4 and TL-5 barrier shapes.

2.3 Crash Testing of Steel and GFRP Reinforced Barrier

Crash testing serves as an important tool to test structural and passenger safety adequacy of various barrier designs with varying materials. Specifically, crash testing has been used to improve upon existing barrier geometry and design, as well as to test how new reinforcement types perform under load, such as GFRP for example.

2.3.1 Crash Testing of Steel Reinforced Barrier

Rosenbaugh et al. (2007) used data from over 100 previous crash tests to aid in designing a new concrete barrier median system that could safely redirect vehicle types ranging from small cars to fully loaded tractor trailers. Specifically, this median was designed to maximize passenger stability and safety upon a crash by limiting wheel climb and roll, limiting peak impact forces, preventing head slap. This design was also ensured to be economically feasible as an alternative to existing barriers, and to pass structural adequacy. Previous crash tests were studied and compared for different barrier shapes. In particular, data regarding vehicle climb, vehicle roll, and peak impact loads were analyzed. These comparisons provided a basis for selecting the most optimal barrier shape. It was found that vertical faced barriers were the most adequate.

The geometry of the vertical faced barrier was then modified to reduce the risk of head slap. This was done by creating a head ejection envelope from previous crash test data, specifically the lateral ejection of the dummy and its vertical head position taking into account vehicle height, vehicle movement (roll or climb), and the head position relative to the vehicle. Interpolation of the envelope was also done to ensure that it encompassed all vehicle types, since existing tests only took into consideration small cars and pickup trucks. As shown in the Figure 2.4, the barrier geometry was modified by cutting the top of the barrier. This cut conforms to the head ejection envelope, and in turn in the event of a crash, the head of the passenger will not make contact with the barrier wall. Based upon vehicle stability and ease of construction, Option C was deemed to be the best choice for geometrical shape. The steel reinforcement in the barrier was designed to minimize construction costs while providing adequate strength. Finally, a 200 ft section of the constructed barrier was crash tested under TL-5 impact conditions using an 80,000-lb tractor trailer and in compliance with NCHRP Report 350 requirements. All TL-5 impact conditions were satisfied.

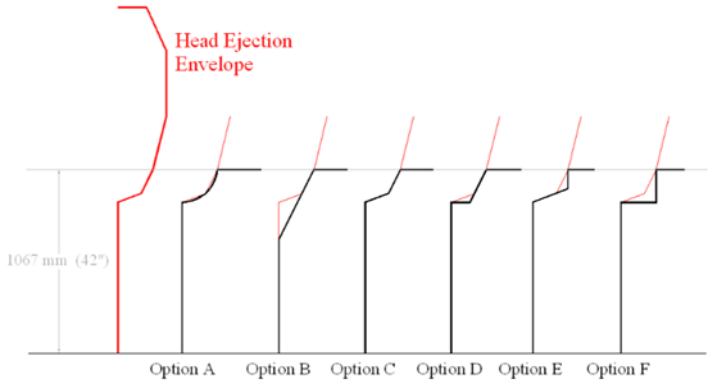

Figure 2.4 Head ejection envelope projection onto various barrier geometries (Rosenbaugh et al., 2007)

2.3.2 Crash Testing of GFRP Reinforced Barrier

T202 Bridge Rail

A crash test was performed by the Texas Transport Institute to investigate the behavior of GFRP reinforced bridge rails (TXDOT T203) under vehicular loading (Buth et al., 2002). Two types of crash tests were carried out. The first type was to study T203's performance based on its strength immediately after construction, and the second type was to study its performance under reduced-strength due to deterioration caused by long periods of exposure to the environment. To consider the life cycle of GFRP reinforcement, two environmental coefficients were used, namely: C_E of 0.7 which represents expected life-cycle deterioration, was used for the first test, and C_E of 1.0 which represents no deterioration, was used in the latter test.

The first test confirmed adequate structural performance, however the vehicle rolled which deemed the safety aspect of the rail inadequate. For the second test, the height of the rail was increased to a height of 30 inches. The second test passed under both structural and safety standards. It was concluded that the weaker section of the railing ($C_E = 1.0$) with added structural steel tube (making the total height 30 inches) proved to have improved vehicle roll stability was well as adequate structural capacity.

TL-5 Barrier

Crash tests were performed on a TL-5 barrier type using GFRP on both the back and front faces of the barrier, using headed bars to ensure proper development length of the wall into the slab (Sennah & Hedjazi, 2018). This barrier-deck slab system was constructed as per MASH test procedure and evaluation criteria. The specific vehicle type used for loading was a 36 000 V tractor trailer which impacted the barrier at 80 km/h at an angle of 15°. Figure 2.5 shows the test schematic and vehicle impact location.

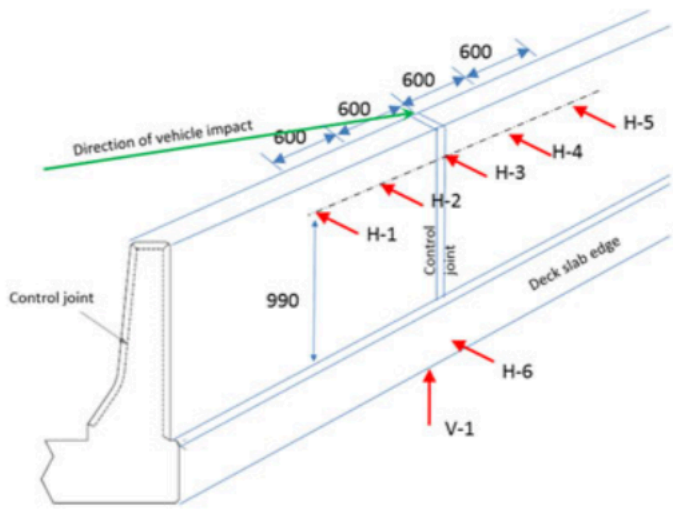

Figure 2.5 TL-5 barrier crash test schematic (Sennah and Hedjazi, 2018)

In Figure 2.5, H-1 to H-6 represent six LVDT sensors which measure the horizontal displacement of the barrier wall, while V-1 represents and LVDT sensor which measures the vertical deflection of the deck slab cantilever. The control joints were included while casting the barrier wall in accordance with the MTO to reduce shrinkage cracks. The crash test conclude that vehicle did not penetrate or go over the barrier wall. The safety aspect of the impact passed as a result of no detached barrier fragments found and no evidence found of barrier debris penetrating the vehicle occupant compartment. Secondly no deformation of the occupant compartment during the test. Also, the vehicle remained upright during the entire duration of the crash. The maximum equivalent static impact load of 559.61 kN was calculated from the acceleration-time history recorded during the crash test.

2.4 Yield Line Analysis of Steel-Reinforced Barrier

AASHTO-LRFD Bridge Design Specifications specify a triangular yield line pattern within the height of the barrier wall to determine its flexural capacity due to vehicle collision. However, recent tests show that a trapezoidal yield line pattern occurs in the steel-reinforced TL-5 barrier upon failure (Fadaee et al., 2018).

2.4.1 AASHTO Triangular Yield-Line Pattern

Figures 2.6 and 2.7 show a typical AASHTO-LRFD triangular yield line pattern at an interior region and end region of a barrier, respectively. Figure 2.6 shows two diagonal yield-lines meeting at the barrier-deck interface with the tension crack being on the traffic side (impact side) of the wall. At the compression side of the wall (back side) there is a vertical yield-line centered at the vehicle impact point. A similar scenario exists for end loading but having only one diagonal yield-line extending down to the wall-deck connection, as shown in Figure 2.7.

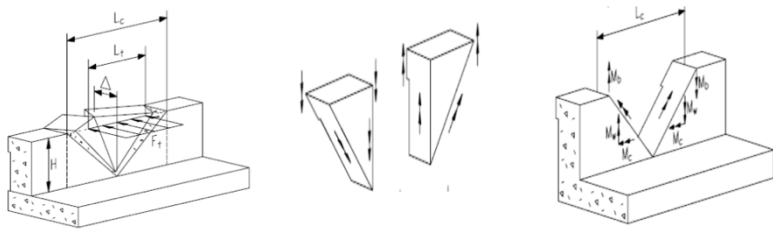

Figure 2.6 Triangular yield line pattern at interior location (Adopted from AASHTO, 2017)

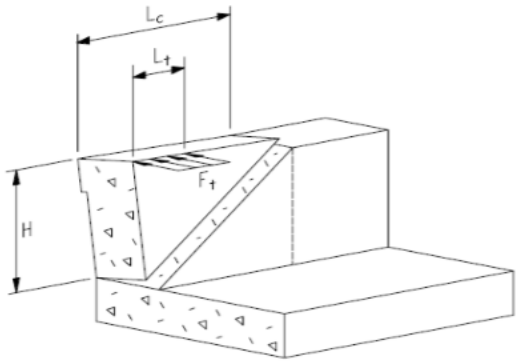

Figure 2.7 AASHTO-LRFD triangular yield line pattern at end location (adopted from AASHTO, 2017)

2.4.2 Development and Explanation of Trapezoidal Yield-Line Failure

The trapezoidal yield-line pattern consists of two diagonal yield lines (one on each side of the transverse loading) extending a horizontal yield-line across the wall-deck interface as shown in Figure 2.8 (Fadaee et al., 2018). At the back side of the barrier wall, two vertical yield-lines exist, one at each boundary location of the transverse load.

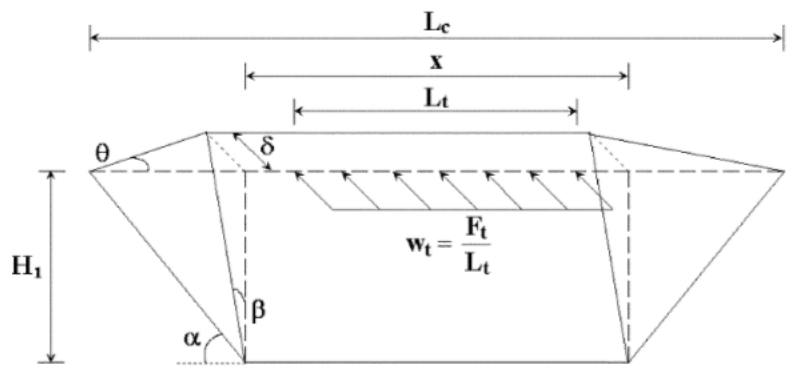

Figure 2.8 Trapezoidal yield-line pattern at interior location (Fadaee et al., 2018)

Regarding the length of the horizontal yield line X, three different scenarios can be considered with respect to loading length, L_t:

Case (a) $X > L_t$

Case (b) $X = L_t$

Case (c) $X < L_t$

***Case (a) and (b)* at Interior Location of Barrier ($X \geq L_t$)**

Figure 2.9 shows the trapezoidal yield line pattern at interior location When $X > L_t$ (Fadaee et al., 2018). The length X can be represented by a factor n_1, where ($1 \leq n_1 \leq 2$) multiplied by the length of the transverse load, L_t. The yield line length, L_c, and the barrier transverse flexural capacity, R_w, are shown in equations 2.1 and 2.2, respectively, while Table 2.1 summarizes the definition of the variables in the above equations.

$$L_c = n_1.L_t + \sqrt{(n_1.L_t)^2 + \frac{8M_b.H + 8M_w.H^2 - M_{c,w}.(n_1.L_t)^2}{M_{c,w}}} \quad \text{(Eq. 2.1)}$$

$$R_w = (\frac{1}{L_c - n_1.L_t})(8M_b.H + 8M_w.H + \frac{M_{c,w}.(Lc^2 - n_1.L_t.L_c)}{H} + \frac{(M_{c,base} - M_{c,w}).(n_1.L_t.L_c - n_1^2.L_t^2)}{H}) \quad \text{(Eq. 2.2)}$$

Table 2.1 Explanation of variables in trapezoidal yield line analysis

Symbol	**Meaning**
X	Length of horizontal yield line
L_t	Length of transverse line load
L_c	Critical length
F_t	Impact load
w_t	Total external work due to applied load
H	Height of barrier wall
R_w	Transverse impact load resistance
M_b	Flexural resistance of cap beam (if applicable)
M_w	Flexural resistance of barrier about its vertical axis
$M_{c,\,w}$	Flexural resistance of barrier about its horizontal axis at the wall
$M_{c,\,base}$	Flexural resistance of barrier about its horizontal axis at the base
δ	Transverse displacement of wall due to applied load
α, β, θ	Various angles as shown in Figure 2. 8

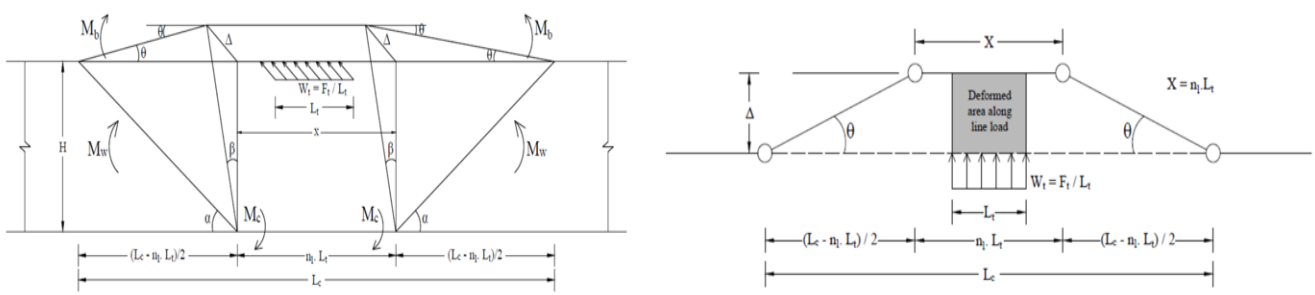

Figure 2.9 Trapzoidal yield line pattern at interior location when X > L_t (Fadaee et al., 2018)

***Case (a) and (b)* at End Location of Barrier ($X \geq L_t$)**

Figure 2.10 shows the trapezoidal yield line pattern at end location When $X > L_t$ (Fadaee et al., 2018). The length X can be represented by a factor n_1, where ($1 \leq n_1 \leq 2$) multiplied by the length of the transverse load, L_t. The yield line length, L_c, and the barrier transverse flexural capacity, R_w, are shown in equations 2.3 and 2.4, respectively. As seen in Figure 2.10, this yield line pattern has a horizontal flexural crack at the barrier base that is propagated diagonally to the top of the barrier wall in the traffic side. This is in addition to a vertical crack at the back face of the barrier.

$$L_c = n_1.L_t + \sqrt{(n_1.L_t)^2 + \frac{M_b.H + M_w.H^2 - M_{c,w}.(n_1.L_t)^2}{M_{c,w}}} \quad \text{(Eq. 2.3)}$$

$$R_w = (\frac{1}{L_c - n_1.L_t})(M_b.H + M_w.H + \frac{M_{c,w}.(Lc^2 - n_1.L_t.L_c)}{H} + \frac{(M_{c,base} - M_{c,w}).(n_1.L_t.L_c - n_1^2.L_t^2)}{H}) \quad \text{(Eq. 2.4)}$$

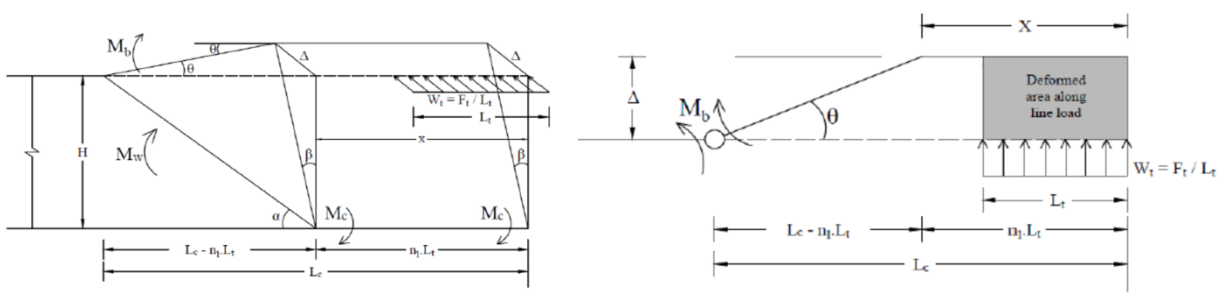

Figure 2.10 Trapzoidal yield line pattern at end location when $X > L_t$ (Fadaee et al., 2018)

***Case (c)* at Interior Location of Barrier ($X < L_t$)**

Figure 2.11 shows the trapezoidal yield line pattern at interior location When $X < L_t$ (Fadaee et al., 2018). The length X can be represented by a factor n_2, where ($0 \leq n_2 \leq 1$) multiplied by the length of the transverse load, L_t. The yield line length, L_c, and the barrier transverse flexural capacity, R_w, are shown in equations 2.5 and 2.6, respectively.

$$L_c = 0.5L_t(1+n_2^2) + \sqrt{0.25L_t^2(1+n_2^2)^2 + \frac{16M_b.H + 16M_w.H^2 - M_{c,w}.(n_2.L_t^2 + n_2^3.L_t^2) - (M_{c,base} - M_{c,w}).(2n_2^2L_t^2 - n_2.L_t^2 - n_2^3.L_t^2)}{2M_{c,w}}} \quad \text{(Eq. 2.5)}$$

$$R_w = \left(\frac{1}{2L_c - L_t - n_2^2.L_t}\right)\left(16M_b.H + 16M_w.H + \frac{2M_{c,w}.(Lc^2 - n_2.L_t.L_c)}{H} + \frac{2(M_{c,base} - M_{c,w}).(n_2.L_t.L_c - n_2^2.L_t^2)}{H}\right) \quad \text{(Eq. 2.6)}$$

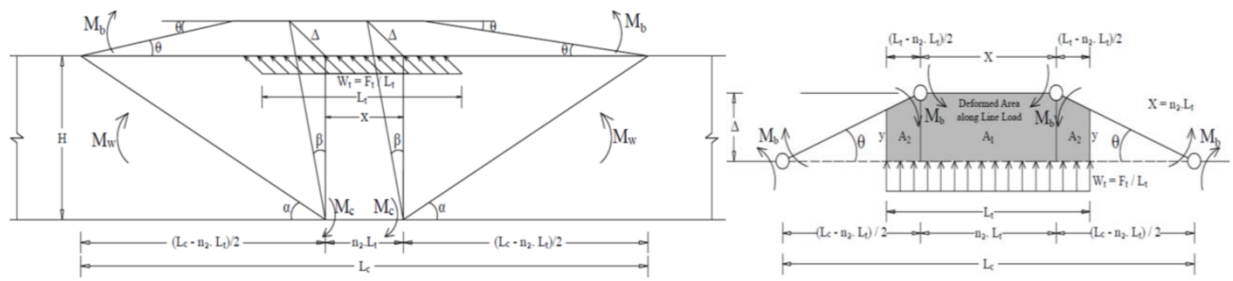

Figure 2.11 Trapzoidal yield line pattern at interior location when X < L_t (Fadaee et al., 2018)

Case (c) at End Location of Barrier (X < L_t)

Figure 2.12 shows the trapezoidal yield line pattern at end location When X < L_t (Fadaee et al., 2018). The length X can be represented by a factor n_2, where ($0 \le n_2 \le 1$) multiplied by the length of the transverse load, L_t. The yield line length, L_c, and the barrier transverse flexural capacity, R_w, are shown in equations 2.7 and 2.8, respectively.

$$L_c = 0.5L_t(1+n_2^2) + \sqrt{0.25L_t^2(1+n_2^2)^2 + \frac{2M_b.H + 2M_w.H^2 - M_{c,w}.(n_2.L_t^2 + n_2^3.L_t^2) - (M_{c,base} - M_{c,w}).(2n_2^2L_t^2 - n_2.L_t^2 - n_2^3.L_t^2)}{2M_{c,w}}} \quad \text{(Eq. 2.7)}$$

$$R_w = \left(\frac{1}{2L_c - L_t - n_2^2.L_t}\right)\left(2M_b.H + 2M_w.H + \frac{2M_{c,w}.(Lc^2 - n_2.L_t.L_c)}{H} + \frac{2(M_{c,base} - M_{c,w}).(n_2.L_t.L_c - n_2^2.L_t^2)}{H}\right) \quad \text{(Eq. 2.8)}$$

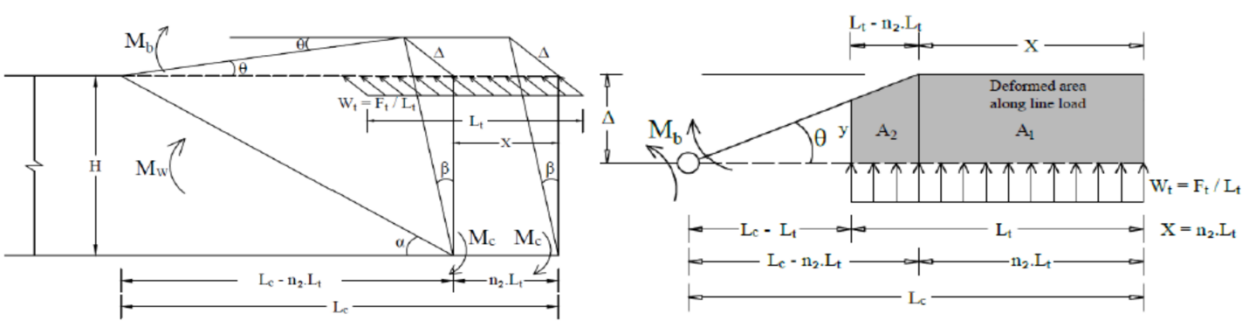

Figure 2.12 Trapzoidal yield line pattern at end location when X < L_t (Fadaee et al., 2018)

2.4.3 TL-5 Barrier Conclusions Using Trapezoidal Yield-Line Failure

Fadaee et al. (2018) performed analysis of the transverse capacity of TL-5 barrier using reinforcing steel bars with different vertical and horizontal spacings, and different values of n_1 and n_2 with increments of 0.5 to determine their proper values to yield the lowest transverse flexural resistance of the barrier wall. Table 2.2 summarizes the parameters considered for their analysis.

Table 2.2 Summary of analysis cases for TL-5 barrier using trapezoidal yield line analysis (Fadaee et al., 2018)

Test Level	**Location**	**Height Evaluated**	**(n_1 or n_2)**	**Horizontal Rebar Spacing – S_h (mm)**	**Horizontal Rebar Spacing – S_v (mm)**
TL-5	Interior	Full Height	n_1: 0.05 Increments from 1 to 2 (21 cases)	100	100
				150	150
	Exterior	Top Tapered Portion	n_2: 0.05 Increments from 0 to 1 (21 cases)	200	200
				250	250
				300	300

2.5 Punching Shear Capacity of Steel-Reinforced Concrete Slabs

Using the existing equations used to determine punching shear capacity of two-way, steel-reinforced concrete slabs serves as the initial point in the analysis for determining suitable equations to predict punching shear capacity for barrier walls.

2.5.1 CSA-A23.3 (2004)

The Canadian Standard *"Design of Concrete Structures"* (CSA Group, 2004) specifies the punching shear capacity of a steel-reinforced two-way concrete slab without shear reinforcement as the minimum of:

$$V_c = (1 + 2 / \beta_c).0.19\lambda\varphi_c. \sqrt{f'_c} . b_{o,0.5d}.d \quad \text{(Eq. 2.9)}$$

$$V_c = [(\alpha_s.d / b_{o,\ 0.5d}) + 0.19]. \lambda\varphi_c.\sqrt{f'_c}\ b_{o,0.5d}.d \quad \text{(Eq. 2.10)}$$

$V_c = 0.38\lambda\varphi_c .\sqrt{f'_c}. b_{o,0.5d}.d$ (Eq. 2.11)

Where: β_c = the ratio of the long side to short side of the concentrated load or loading patch

λ = concrete density (taken as 1 for normal density concrete)

φ_c = concrete resistance factor (taken as 0.75 in accordance with CHBDC and 0.65 in accordance with CSA-A23.3 (2004)

f'_c = 28-day concrete compressive strength

$b_{o,0.5d}$ = critical perimeter measured at a distance 0.5d to the loading patch area

d = effective depth of concrete section

α_s = factor to adjust V_c for support dimensions (4 for interior columns, 3 for edge columns and 2 for corner columns)

2.5.2 ACI 318 (2005)

The American Standard "*Building Code Requirements for Structural Concrete and Commentary"* (American Concrete Institute, 2005) specifies the punching shear capacity of a non-prestressed steel-reinforced concrete slabs as the minimum of the following equations:

$V_c = (2 + 4 / \beta_c).\sqrt{f'_c} . b_{o,0.5d}.d$ (Eq. 2.12)

$V_c = [(\alpha_s.d / b_{o,\ 0.5d}) + 2].\sqrt{f'_c}\ b_{o,0.5d}.d$ (Eq. 2.13)

$V_c = 4.\sqrt{f'_c}. b_{o,0.5d}.d$ (Eq. 2.14)

Where: α_s = factor to adjust V_c for support dimensions (40 for interior columns, 30 for edge columns and 20 for corner columns)

2.5.3 JSCE (2007)

The Japanese Standard "*Standard Specifications for Concrete Structures"* (Japanese Society of Civil Engineering (JSCE), 2007) provides an empirical-based equation to determine punching shear capacity for planar members. This Standard provision takes into account the reinforcement

ratio of the section which is equal to the average reinforcement ratio of both directions. The punching shear equation is as follows:

$V_c = \beta_d . \beta_p . \beta_r . (f_{pcd} / \gamma_b) . b_{o,0.5d} . d$ (Eq. 2.15)

Where: $\beta_d = \sqrt[4]{\frac{1000}{d}} \leq 1.5$ (d in mm)

$\beta_p = (100\,\rho)^{1/3} \leq 1.5$ (ρ = average reinforcement ratio of section)

$\beta_r = 1 + \frac{1}{[1+0.25\left(\frac{u_o}{d}\right)]}$

u_o = perimeter of concentrated load area

$f_{pcd} = 0.2\sqrt{f'_c} \leq 1.2$ in MPa

γ_b = partial safety factor to account for concrete compressive strengths (1.3 for strength < 50MPa and 1.5 for strength > 50 MPa).

2.5.4 Eurocode-2 (2004)

The European Standard "*Design of Concrete Structures*" (Eurocode 2, 2004) provides an empirical-based equation to determine punching shear capacity for a steel reinforced concrete slab. Similar to JSCE (2007), this developed equation considers the average reinforcement ratio in both directions.

$V_c = 0.25\,(f_{ctk} / \gamma_c) . K_{EC} . (1.2 + 40\rho) . b_{o,1.5d} . d$ (Eq. 2.16)

Where: $f_{ctk} = 0.7 f_{ctm}$

$f_{ctm} = 0.3\,(f_{ck})^{2/3}$ (f_{ck} in MPa)

f_{ck} = characteristic concrete compressive strength

$K_{EC} = (1.6 - d) \geq 1$ (d in meters)

$\rho = \sqrt{\rho x \rho y} \leq 0.15$ (ρ_x and ρ_y are reinforcement ratios in longitudinal and transverse directions, respectively)

γ_c = partial factor of safety, set equal to 1 to determine an un-factored prediction capacity to be compared with experimental punching shear.

2.5.5 British Code-1997 (BS 8110)

The British Standard 8110 "*Structural Use of Concrete-Code of Practice for Design and Construction"* (BS 8110, 1997) specifies the punching shear capacity of a steel-reinforced concrete slab as follows:

$$V_c = 0.79K_1(K_2/\gamma_m).(100\rho)^{1/3}.(400/d)^{1/4}.\ b_{o,1.5d}.d \qquad \text{(Eq. 2.17)}$$

$$V_c \leq 0.80\sqrt{f_{ck}}.\ b_{o,1.5d}.d \leq 5\ b_{o,1.5d}.d \qquad \text{(Eq. 2.18)}$$

Where: $K_2 = (f_{ck}/25)^{1/3} \geq 1$ (f_{ck} in MPa)

$(400/d) \geq 1$ (d in mm)

$0.0015 \leq \rho \leq 0.03$

γ_m = partial factor of safety, set equal to 1 to determine an un-factored prediction capacity to be compared with experimental punching shear.

K_1 = variable enhancement factor for support compression and is set conservatively to 1.

2.5.6 CEB-FIP Model Code 1990 (MC90)

The European Code (MC90) "*Design Code for Concrete"* (CEB-FIP, 1993) specifies the punching shear capacity of a steel-reinforced concrete slab as follows:

$$V_c = 0.12.\xi.(100\rho\ f_{ck})^{1/3}.\ b_{o,2d}.d \qquad \text{(Eq. 2.19)}$$

Where: $\xi = 1 + (0.2/d)^{1/2}$ (d in m, f_{ck} in MPa)

A partial factor of safety was likely used as part of the constant 0.12 in the above equation (Matthys & Taerwe, 2000). To determine an un-factored punching shear capacity, this factor was multiplied by a partial safety factor of 1.5. In turn, the constant was changed to 0.18.

2.6 Punching Shear Capacity of Steel-Reinforced and GFRP-Reinforced Barrier

The following subsections provide summary of the punching shear capacity equations developed based on the experimental findings.

2.6.1 Punching Shear Capacity of GFRP-Reinforced Barrier

Since the mechanical properties of GFRP bars are different than steel bars, the punching shear equations used for steel bars must be modified to accurately determine barrier punching shear capacity containing GFRP bars. Specifically, these modified equations account for the lower elastic modulus, lower transverse shear strength, and higher tensile strength with no yielding point, found in GFRP bars. With the lower elastic modulus present in GFRP bars compared to steel bars, the neutral axis location of a cracked section with GFRP will change significantly (decrease in depth) compared to a section containing steel reinforcement. As a result, the reinforcement ratio of a GFRP section plays a major role in accurately determining its punching shear capacity. To help develop these modifications, punching shear capacities were predicted using equations from different design codes as well as various empirical formulas developed from past research which account for reinforcement ratios when determining punching shear capacities of a two-way slab with GFRP bars (Khederzadeh and Sennah, 2014). Table 2.3 shows the calculated punching capacities compared with the experimental punching shear capacities.

Table 2.3 Comparison of theoretical punching shear capacites with expermental punching shear capacities (Khederzadeh & Sennah, 2014)

Barrier Designation	**$V_{c,\ test}$ (kN)**	**$V_{c,\ test}$ / $V_{c,\ pred.}$**								
		$V_{c,\ S806}$	**$V_{c,\ ACI\ 440}$**	**$V_{c,\ JSCE}$**	**$V_{c,\ EGA\ 1999}$**	**$V_{c,\ EGA\ 2000}$**	**$V_{c,\ MT}$**	**$V_{c,\ OSP}$**	**$V_{c,\ EGM}$**	**$V_{c,\ JCOB}$**
P3GFI-PU	654.9	2.05	1.79	1.03	0.77	1.17	1.46	1.07	1.19	1.29
P3GFI1-SH	621	1.94	1.70	0.97	0.73	1.11	1.38	1.01	1.13	1.23
P3GFI2- SH**	607	1.90	1.66	0.95	0.71	1.08	1.36	0.99	1.10	1.20
	Mean	**1.96**	**1.71**	**0.983**	**0.74**	**1.12**	**1.4**	**1.02**	**1.14**	**1.24**
	SD	0.078	0.07	0.042	0.031	0.046	0.053	0.042	0.05	0.05
	COV %	3.95	3.87	4.23	4.14	4.10	3.78	4.07	4.02	3.69
P3GFE1-PU*	463.3	1.34	1.07	0.66	0.63	0.83	1.04	0.76	0.73	1.04
P3GFE2-PU	541.2	1.56	1.25	0.77	0.73	0.97	1.22	0.88	0.86	1.21
P3GFE-SH	593	1.71	1.37	0.84	0.81	1.06	1.33	0.97	0.94	1.33
	Mean	**1.52**	**1.23**	**0.76**	**0.723**	**0.95**	**1.19**	**0.87**	**0.84**	**1.19**
	SD	0.186	0.151	0.091	0.090	0.116	0.146	0.105	0.11	0.15
	COV %	12.11	12.27	11.99	12.47	12.16	12.23	12.11	12.6	12.2

In turn, it was concluded that the punching shear model by Jacobsen et al. equation (Jacobson et al., 2005) showed the best correlation with the experimental punching shear capacity.

2.6.2 Punching Shear Capacity of Steel-Reinforced Barrier

Unlike a cracked GFRP-reinforced concrete section, a cracked steel concrete section has very little effect in changing the depth of its neutral axis. This is due to steel having a significantly higher elastic modulus than that of GFRP. As a result, the punching shear capacity of a steel barrier does not need to take into account the average tensile reinforcement ratio as discussed in the previous section. Based on comparison with the experimental capacities, it was found that CSA-A23.3 (CSA Group, 2004) provided the most accurate prediction. However, referring to Figure 2.13, experimental results showed that critical perimeter bo was approximately 1.5d, rather than 0.5d used in CSA-A23.3 (2004). As a result, the CSA-A23.3 equation was modified as shown in equation 2.20. Table 2.4 summarizes the accuracy of the proposed punching shear capacity with the obtained experimental capacity.

$$V_c = (1 + 2 / \beta_c).0.146\lambda\varphi_c. \sqrt{f'_c} . b_o,1.5d.d \qquad \text{(Eq. 2.20)}$$

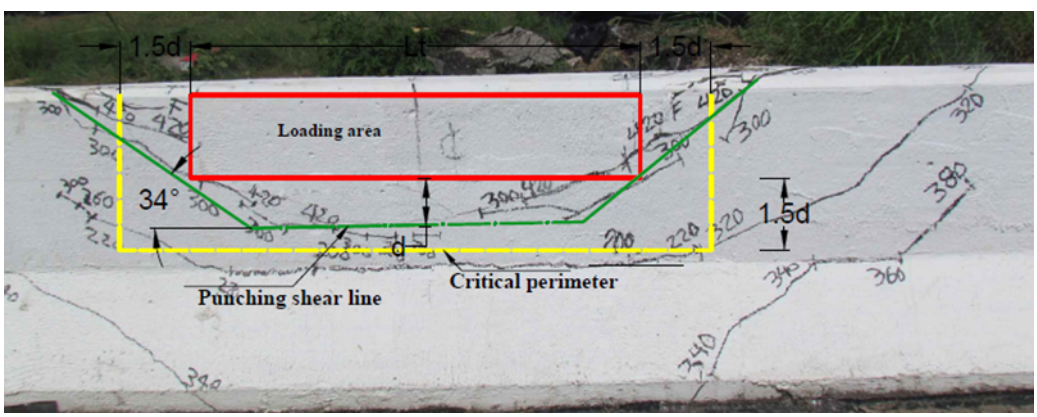

Figure 2.13 Visual illustration of critical shear perimeter on tested barrier wall (Khederzadeh & Sennah, 2014)

Table 2.4 Experimental and proposed punching shear capacities of the tested barriers (Khederzadeh & Sennah, 2014)

Load location		$V_{c,\ test}$ (kN)	$V_{c,\ proposed}$ (kN)	$V_{c,\ test}$ / $V_{c,\ proposed}$ ratio
TL-5 Barrier	Interior location	885.9	730.6	1.21
	Exterior location	627.13	576.96	1.09
TL-4 Barrier	Interior location	421.9	318.2	1.32
	Exterior location	243.66	229.9	1.06

2.7 Repair of Deteriorated or Damaged Barriers

2.7.1 Repair of GFRP-Reinforced Concrete Barriers Using Planting and NSM Methods

Currently, CHBDC provides guidelines for design of concrete barriers reinforced with GFRP bars, however no guidelines exist for repair of these structures. Elsalakawy and Rubiat Islam (El-Salakawy & Rubiat Islam, 2014) conducted research which evaluated how feasible and efficient current repair techniques are on barriers reinforced with GFRP bars. Their study consisted of 3 full-scale TL-4 barriers that were 6 m in length reinforced entirely reinforced with GFRP bars and statically loaded to simulate a vehicle crash test. The loads were applied at interior and exterior locations of the barriers. A previous study was done employing concrete demolition methods such as water blasting and jack hammering. However, these two methods resulted in severe damage to the existing GFRP reinforcement. It was then determined that the damaged wall should be saw-cut, and the affected reinforcement be replaced with new GFRP either by using near-surface-mounting (NSM) shown in Figures 2.14 and 2.16 or planting (splicing method) as shown in Figures 15 and 17. Their investigation compared the structural performance before and after the repairs to determine the adequacy of each repair type. Table 2.5 summarizes the failure load of each sample before and after repair. It can be seen that using either NSM or planting method on the barriers loaded at the interior location (M1-C and M2-C), yields a higher failure load than that obtained on the original sample. However, for the sample loaded at the end locations (E1-C and E2-C), the repaired barrier failure loads were approximately 8% less than that of the control sample. It can also be concluded that samples repaired using NSM resisted approximately 10% of higher load than the same samples repaired using the planting method. This is due to the fact that using the NSM method allows for a section to have a greater effective depth than using the planting method.

Table 2.5 Summary of failure load of each sample before and after repair (El-Salakawy & Rubiat Islam, 2014)

Test Designation		**Failure Load (kN) Actual/Normalized**	
Control	**Repaired**	**Control**	**Repaired**
M1-C	M1-P	391/371	348/348
M2-C	M2-N	373/373	451/424
E1-C	E1-P	245/245	208/226
E2-C	E2-N	237/237	230/250

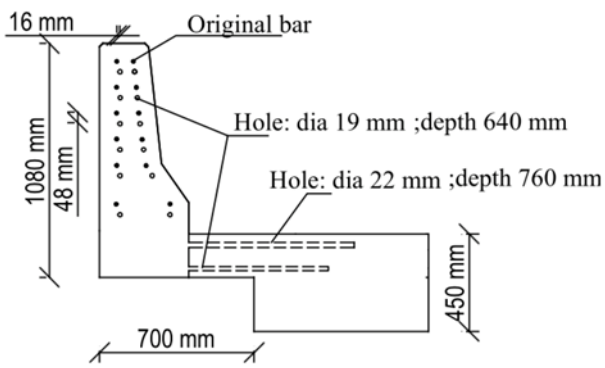

Figure 2.14 Transverse section view of planting method schematic (El-Salakawy & Rubiat Islam, 2014)

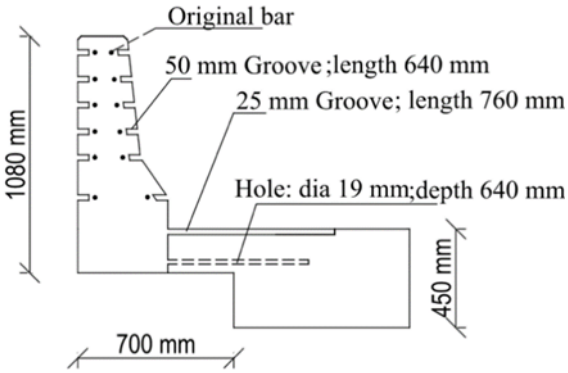

Figure 2.15 Transverse section view of NSM method schematic (El-Salakawy & Rubiat Islam, 2014)

Figure 2.16 Planting method used to replace GFRP at interior location of barrier (El-Salakawy & Rubiat Islam, 2014)

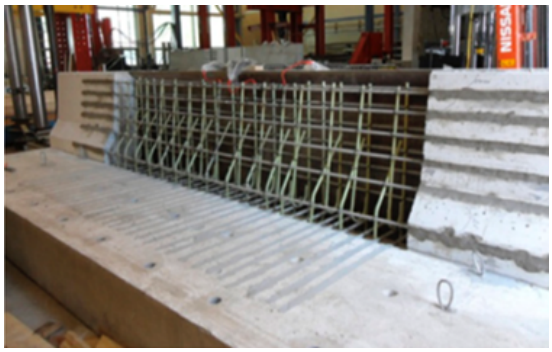

Figure 2.17 NSM method used to replace GFRP at interior location of barrier (El-Salakawy & Rubiat Islam, 2014)

2.7.2 Repair of GFRP-Reinforced Concrete Barriers Using Post-Installed Vertical Reinforcement

A deteriorated GFRP bridge barrier can also be repaired by post-installing reinforcement into the existing deck slab. The damaged barrier section is saw-cut so that just the deck slab remains. The next step is to drill holes in the deck slab at the required embedment length and orientation. An epoxy filling is then inserted into each of the holes, followed by the insertion of the new GFRP bars via a twisting motion. Shown in Figure 2. 18 shows a typical procedure carried out by (Rostami et al., 2017) for post-installing GFRP bars into an existing concrete deck. This repair method was proved to be adequate regarding structural integrity since the experimental ultimate loads of the tested specimens were greater than the CHBDC design values.

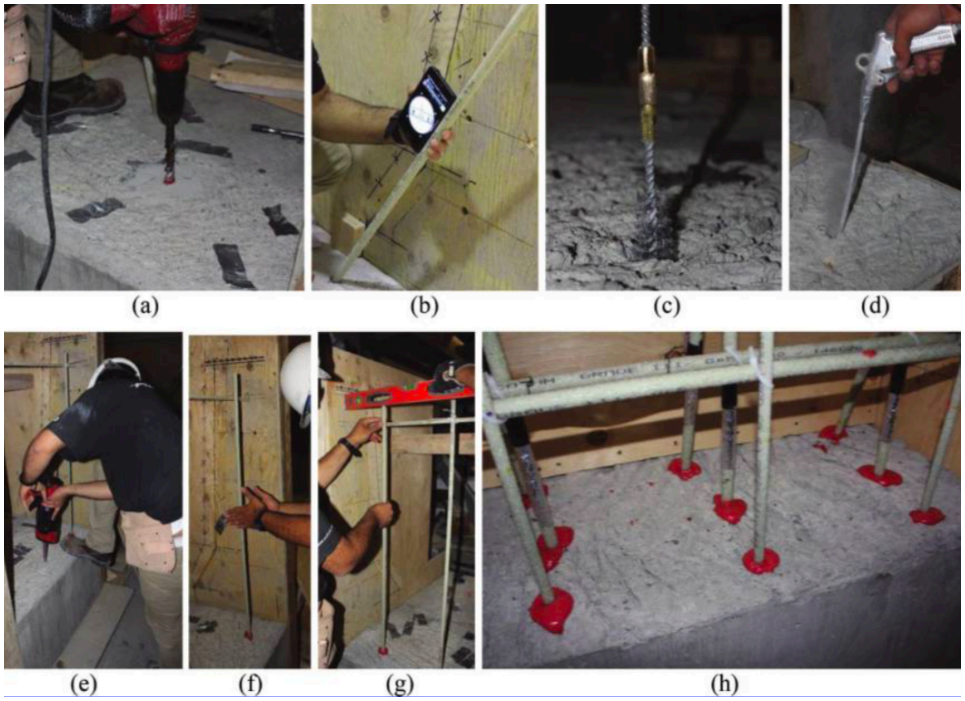

Figure 2.18 Procedure for post-installation of GFRP bars into existing deck (Rostami et al., 2017)

2.8 Fibre-Reinforced Concrete (FRC) Barriers

The use of fibre-reinforced concrete (FRC) for bridge barriers offers advantages over the use traditional concrete. FRC reduces the amount of shrinkage cracks which occur, allows for a reduction in barrier cross-section and reinforcement amount, and limit the crack openings present under service loads (Charron et al., 2011). Charron et al. conducted experimental and numerical

research to verify the performance of precast FRC barriers. Three different FRC samples were constructed with varying percentage of steel fibres (1%, 1.5%, and 4%), concrete strength (50 MPa, 70 MPa, and 120 MPa), and parapet thickness (225 mm, 160 mm, and 95 mm). These samples were compared to an on-site constructed high-performance concrete (HPC) barrier with a concrete strength of 50 MPa. Each sample was tested under static and dynamic conditions using quasi-static loading. The results of both the static and dynamic tests show that each of the FRC barriers yield a higher maximum strength than the HPC barrier, refer to Table 2.6. However, the researchers noted that the HPC barrier was not designed optimally and was included for comparison only.

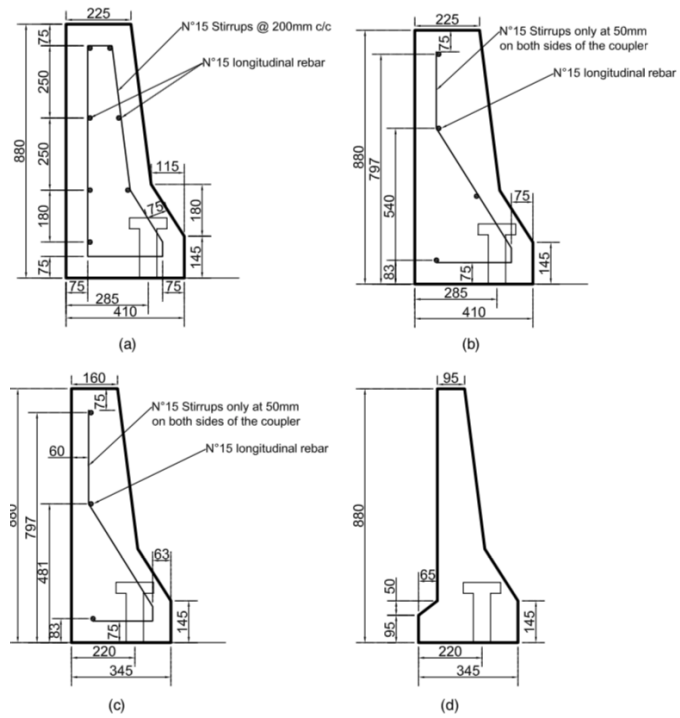

Figure 2.19 Structural design of each precast sample: (a) HPC 50 MPa; (b) FRC 50 MPa-1%; (c) FRC 70 MPa-1.5%; (d) FRC 120 MPa-4% (Charron et al., 2011)

Table 2.6 Summary of specimen strengths under static and dynamic loading (Charron et al., 2011)

Parapet Type	Maximal Strength	Failure Mode	Residual Strength[a]	Failure Mode
HPC 50 MPa Precast	260 kN	Flexural-shear	245 kN	Flexural-shear
FRC 50 MPa-1% Precast	360 kN	Flexural-shear	306 kN	Flexural-shear
FRC 70 MPa-1.5% Precast	350 kN	Flexural	260 kN	Flexural-shear
FRC 120 MPa-4% Precast	320 kN	Flexural	320 kN	Flexural-shear

[a]Maximal strength measured with quasi-static test after the four levels of impact.

The results in Table 2.6 indicate that all FRC barriers structurally adequate under static load as per CSA (2006), MTQ (2006), and AASHTO (2007). Similarly, all the residual strength of each FRC barrier was deemed adequate as per AASHTO (1989) and NCHRP (1993). However, the HPC sample was deemed structurally inadequate. In addition to determining structural performance, efficiency of each sample in terms of cost, strength, and construction time was also studied. Table 2. 7 shows a summary of each of the four sample's efficiency under each category. It is evident that the HPC barrier has the lowest cost/strength ratio, however it has a construction time of 4.5 times more than the precast HPC barriers. It is clear that the most optimal barrier is the precast FRC 50 MPa barrier with 1% steel fibers, having significantly faster construction time and the second lowest cost/strength ratio.

Table 2.7 Summary of efficiencies of each barrier (Charron et al., 2011)

Parapet Type	**Cost of One Parapet ($/$)**	**Ultimate Strength (kN/kN)**	**Cost/Strength ($/kN/$/kN)**	**Construction Time 30-m Bridge (days)**
HPC 50 MPa Built on Site	1.0	1.0[a]	1.0	18
HPC 50 MPa Built on Precast	0.94	0.74	1.26	4
FRC 50 MPa-1% Precast	1.16	1.03	1.13	4
FRC 70 MPa-1.5% Precast	1.25	1.01	1.25	4
FRC 120 MPa-4% Precast	4.49	0.92	4.91	4

[a]Theoretical ultimate resistance.

Chapter III

Experimental Program

3.1 Introduction

A total of four full-scale TL-5 concrete barriers were constructed. Two of the specimens were of 4.5 m length to simulate end impact loading and the other two specimens were of 6.5 m length to simulate impact loading at the center of the barrier wall. For both end and center loading, a barrier with a thick slab and a barrier with a cantilevered slab (to simulate barrier overhang) were constructed. Figures 3.1 shows schematic diagrams of TL-5 barrier and thick base dimensionings along with the details of stainless-steel bars used to reinforce the barrier wall and the details of reinforcing streel bars to reinforce the nondeformable concrete base. Figure 3.2 shows similar arrangement for the barrier wall but supported over a deck slab cantilever.

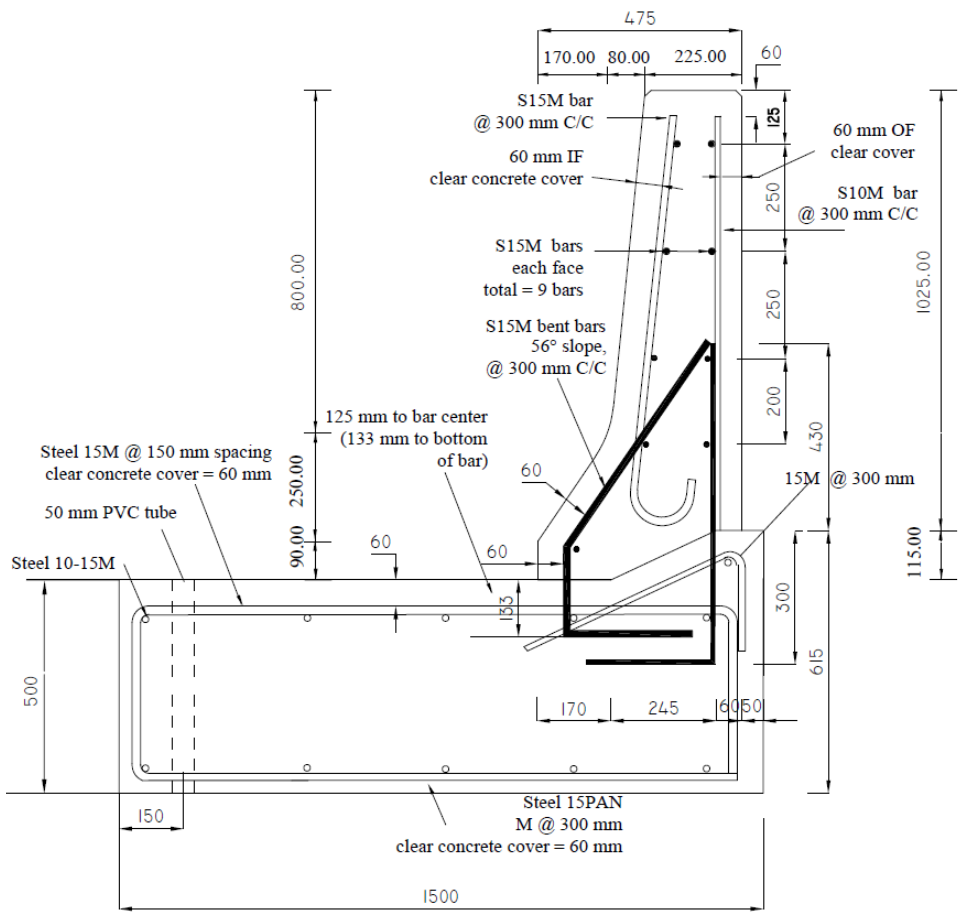

Figure 3.1 Cross-section of barrier specimen with thick base

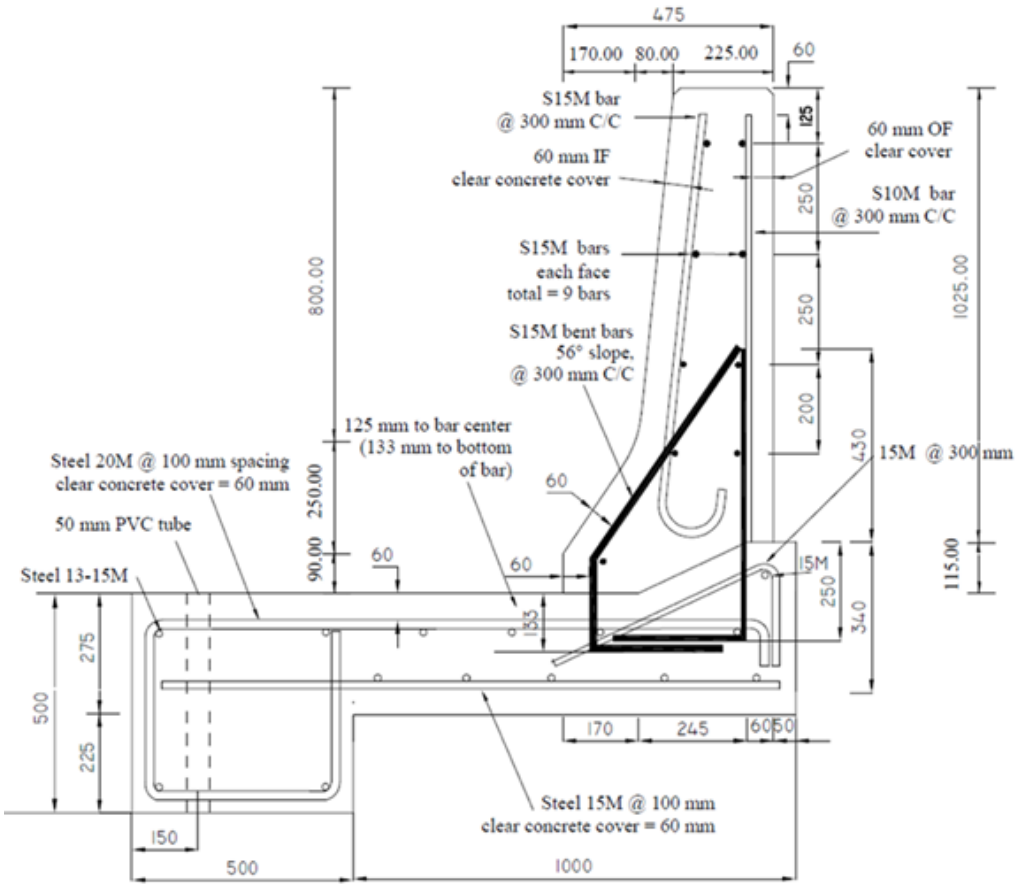

Figure 3.2 Cross-section of barrier specimen with deck slab cantilever

The barrier wall dimensioning and reinforcement were identical to those specified in the Ontario Ministry of Transportation's (MTO) standard drawing for stainless-steel reinforced TL-5 barrier. S15M stainless steel bars at 300 mm spacing were used to reinforce the barrier wall in the vertical direction at the traffic side, while S10M stainless steel bars at 300 mm spacing were used to reinforce the back side of the barrier wall at the back face. Nine S15M stainless steel bars were used to reinforce the barrier wall in the horizontal direction as depicted in Figures 3.1 and 3.2. It should be noted that the vertical reinforcement in the traffic side in case of the 4.5 m long barrier was doubled over a 2.45 m length from the loaded end. A 500 mm concrete base was used in two of the specimens to simulate the bridge barrier mounted over a thick concrete slab, thick voided slab adjacent box beams on which the base under the barrier wall is considered undeformed when the barrier wall is loaded laterally. On the other hand, two specimens were cast using deck slab

cantilever of length 1000 mm as shown in Figure 3.2 to simulate the barrier wall mounted over deck overhang in a slab-on-I-girder bridge system.

3.2 Concrete Strength and Material Properties

Concrete *Standard 35 C1* mix was supplied by Lafarge with the properties shown in Table 3.1. At the time of casting the base as well as the barrier wall, concrete cylinders were cast to assist in determining the concrete strength on the day of testing. They were cured the same amount of time as the barrier specimens (7 days) to ensure accurate representation of concrete compressive strength in the tested barriers. It should be noted that the barrier specimens were cast in two stages, the base followed by the barrier wall with at least two weeks between the times of casting. The concrete surface at the interface between the base and the barrier wall was scratched to allow for greater friction resistance at the interface between the two concretes. Before the testing of each specimen, compression tests were performed on concrete cylinders to determine concrete compressive strength for the slab base and barrier wall.

Table 3.1 Proportions of standard 35 C1 mix for target concrete compressive strength of 35 MPa (supplied by Lafarge Canada Inc., (Lafarge, 2020))

Ingredient	**Quantity**
Cement type GU	390 kg/m^3
Sand	733 kg/m^3
Aggregate 20 mm	1070 kg/m^3
Water	155 L/m^3
Air	6.5 %
MasterGlenium 7700	400.0 mL/m^3
MasterAir	230 mL/m^3
w/cm	0.397

*Notes: BASF – MasterGlenium 7700 is a polycarboxylate-based high-range water-reducing admixture; MasterAir is an air-entraining admixture. Target slump = 150 mm.

Figure 3. 3 A typical concrete cylinder before (left) and after (right) compression test

Figure 3.3 shows a typical concrete cylinder before and after conducting the compression test. According to CHBDC, the equivalent concrete compressive strength used for analysis can be determined from the concrete cylinder compressive strengths as follows:

$$f_c' = 0.9\,\bar{f}_c(1 - 1.28\{(k_c V)^2 / n + 0.0015\}^{0.5}) \qquad \text{(Eq. 3.1)}$$

where $\bar{f}_c$ is the average concrete strength of the tested cylinders, k_c is the coefficient of variation factor for concrete based on number of tested cylinders and as obtained from Table 3.2, n is the number of tested cylinders and V is the coefficient of variation of concrete strength that takes into account the change of strength value of each cylinder from the average strength.

Table 3.2 Coefficient of variation modification factor based on the number of tested concrete cylinders (CSA Group, 2014)

n	2	3	4	5	6	8	10	12	16	20	25+
k_c	2.40	1.47	1.28	1.20	1.15	1.10	1.08	1.06	1.05	1.03	1.02

Table 3.3 summarizes the average strength and characteristic strength of concrete used to cast the concrete base and the barrier wall.

Table 3.3 Properties of concrete used in casting

Specimen #	Concrete segment	Recorded compressive strengths (MPa)	Average compressive strength (MPa)	Characteristic compressive strength (MPa)
S-1	Base	51.823, 53.593, 52.214, 49.132, 54.124	52.266	43.459
	Wall	52.001, 50.677, 50.718, 51.477, 51.208, 51.318, 51.216, 52.856, 52.125, 53.559	51.771	45.023
S-2	Base	50.849, 47.974, 50.828, 47.250, 49.153	49.211	43.761
	Wall	48.781, 51.828, 50.987, 49.463, 51.745, 49.587, 51.490, 49.263, 53.476, 53.207	50.983	45.367
S-3	Base	39.156, 53.655, 27.827, 36.763, 36.694	38.819	33.617
	Wall	37.997, 39.252, 40.528, 39.666, 39.356, 41.024, 38.797, 39.107, 39.647, 41.093	39.647	35.286
S-4	Base	49.850, 49.740, 49.590, 51.400, 49.940	50.104	44.595
	Wall	46.170, 45.850, 47.930, 44.040, 45.160, 49.640, 43.180, 42.700, 46.260, 25.740	43.667	38.588

3.3 Steel Reinforcement Strength and Material Properties

Per the reinforcement details shown in Figures 3.1 and 3.2, stainless steel bars and reinforcing steel bars were ordered with specific bar details shown in Figure 3.4. To verify strength of the steel bars used (regular and stainless-steel), tensile tests were performed on coupons taken from the various rebars. Each coupon was tested under increasing tensile force until fracture. Figure 3.5 shows the stress-strain relationships for 6 reinforcing steel coupon specimens, 3 of which were of 15M size and the other 3 coupons were of 20M size. Figure 3.6 shows views of the tensile test setup with the griped coupons before and after testing. One may observe that bar fracture occurs along the gauge length in some coupons and outside, or at the end of, the gauge length in other coupons. Results show that the average yield strength of the reinforcing steel bars is 480 MPa. Three stainless steel coupons of 15M size and other 3 stainless steel coupons of 10M size were taken from the shipment supplied by Salit Specialty Rebar Inc. The stainless steel used was of 2205 Duplex Stainless steel with other commercial names as UNS S31803 and UNS S32205. Figures 3.7 and 3.8 depict the recorded stress-strain relationships for the tested coupons and the tested

specimens before and after tensile testing. Results show that the average yield strength of the stainless steel is 730 MPa.

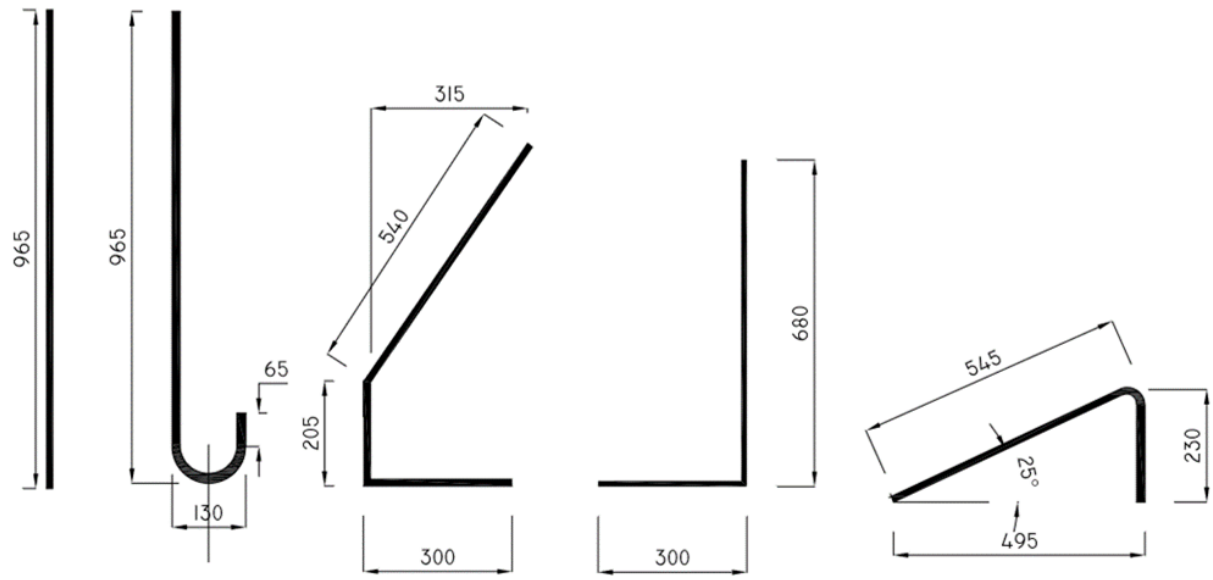

Figure 3.4 Reinforcement details

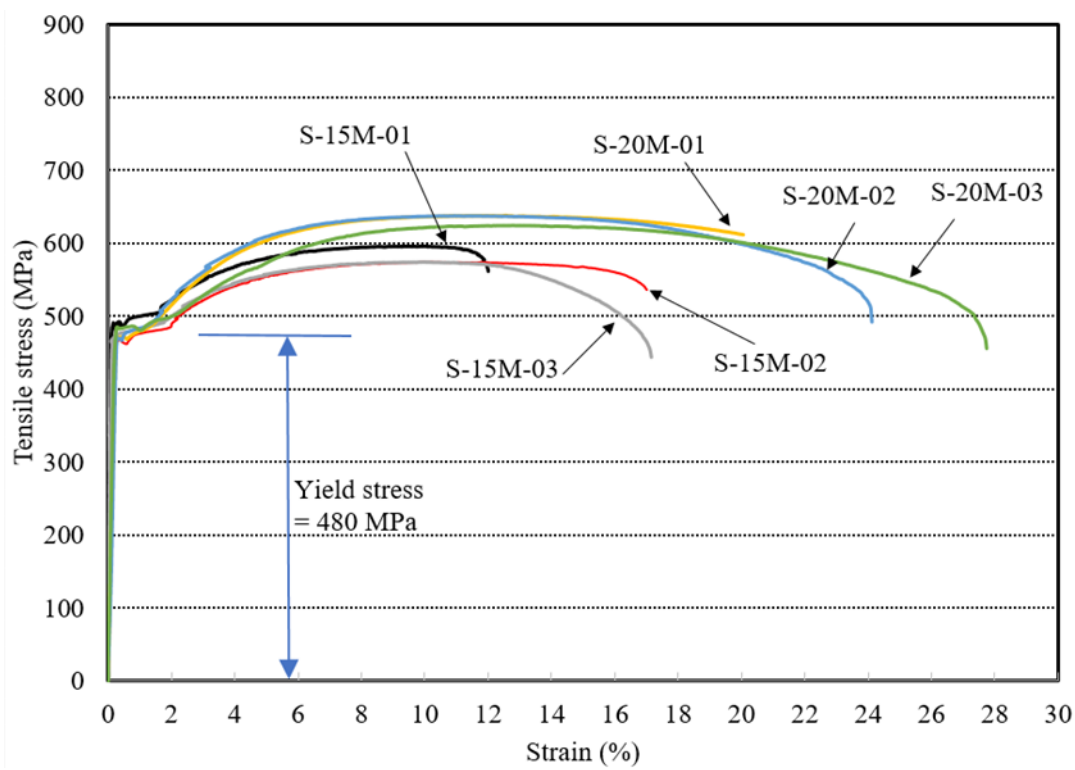

Figure 3.5 Tensile stress-strain relationship for steel bars

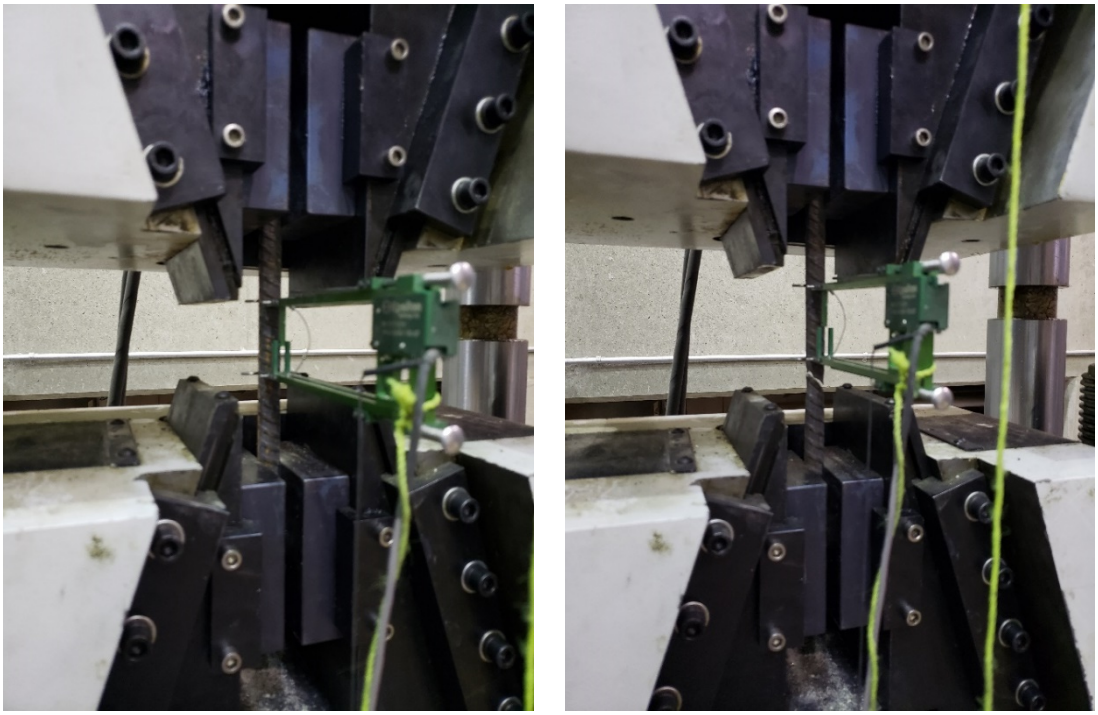

(a) Views of the test setup for 15M reinforcing steel coupon # 1before testing (left) and after failure (right)

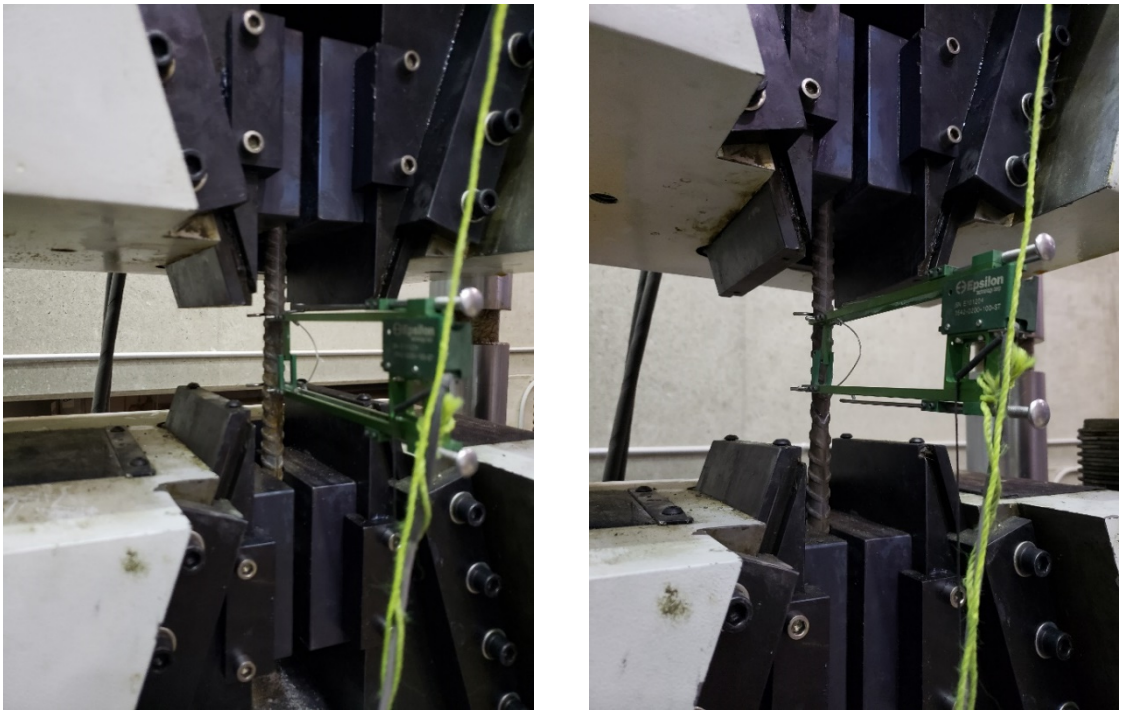

(b)Views of the test setup for 15M reinforcing steel coupon # 2 before testing (left) and after failure (right)

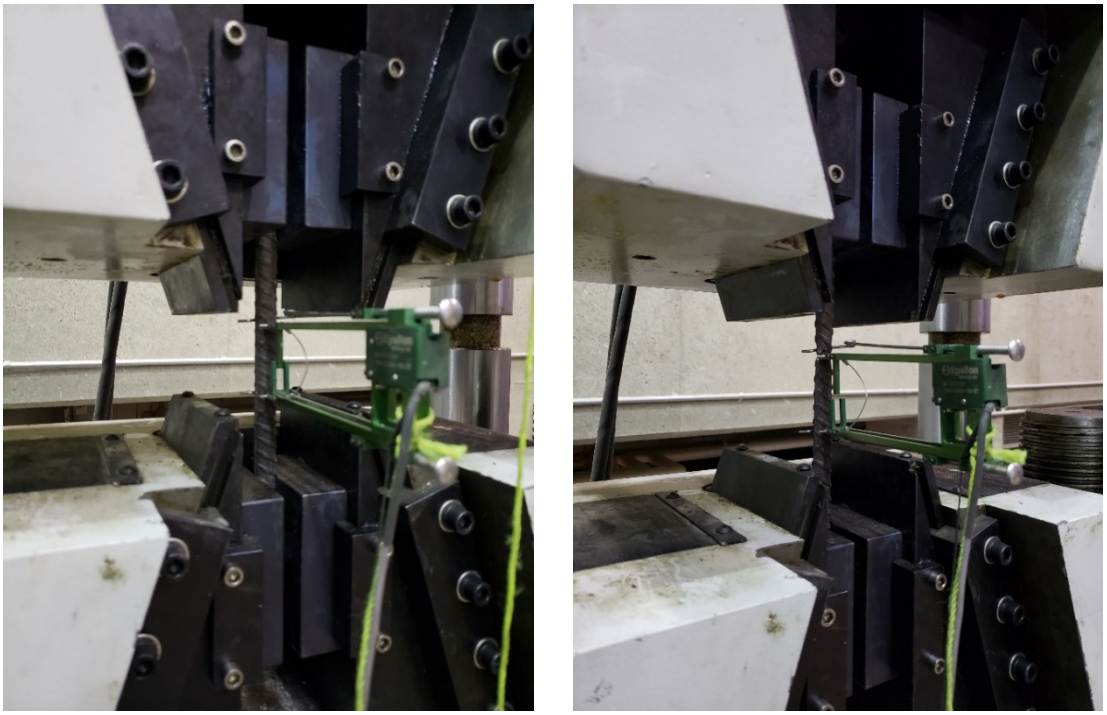

(c) Views of the test setup for 15M reinforcing steel coupon # 3 before testing (left) and after failure (right)

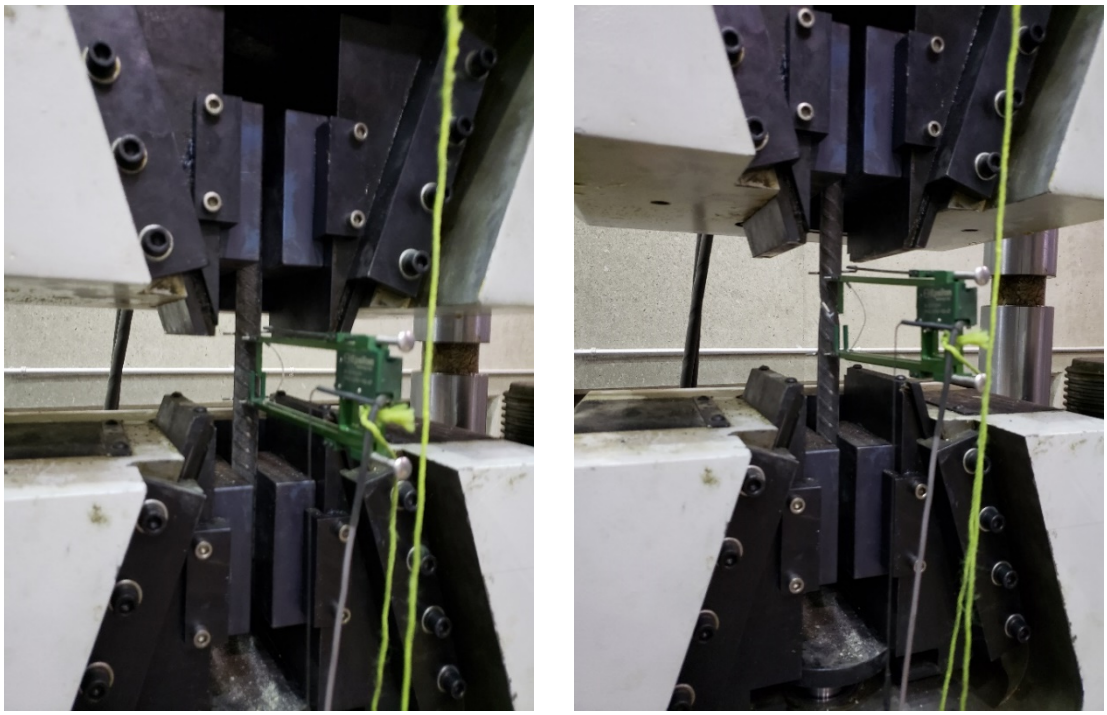

(d) Views of the test setup for 20M reinforcing steel coupon # 1 before testing (left) and after failure (right)

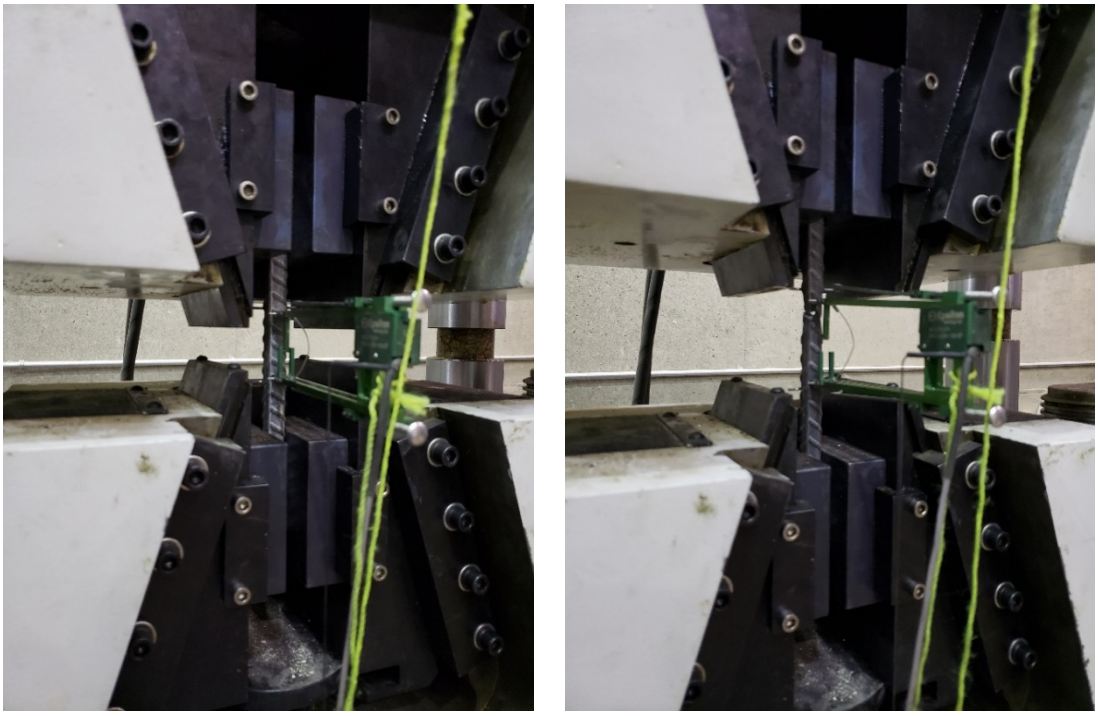

(e) Views of the test setup for 20M reinforcing steel coupon # 2 before testing (left) and after failure (right)

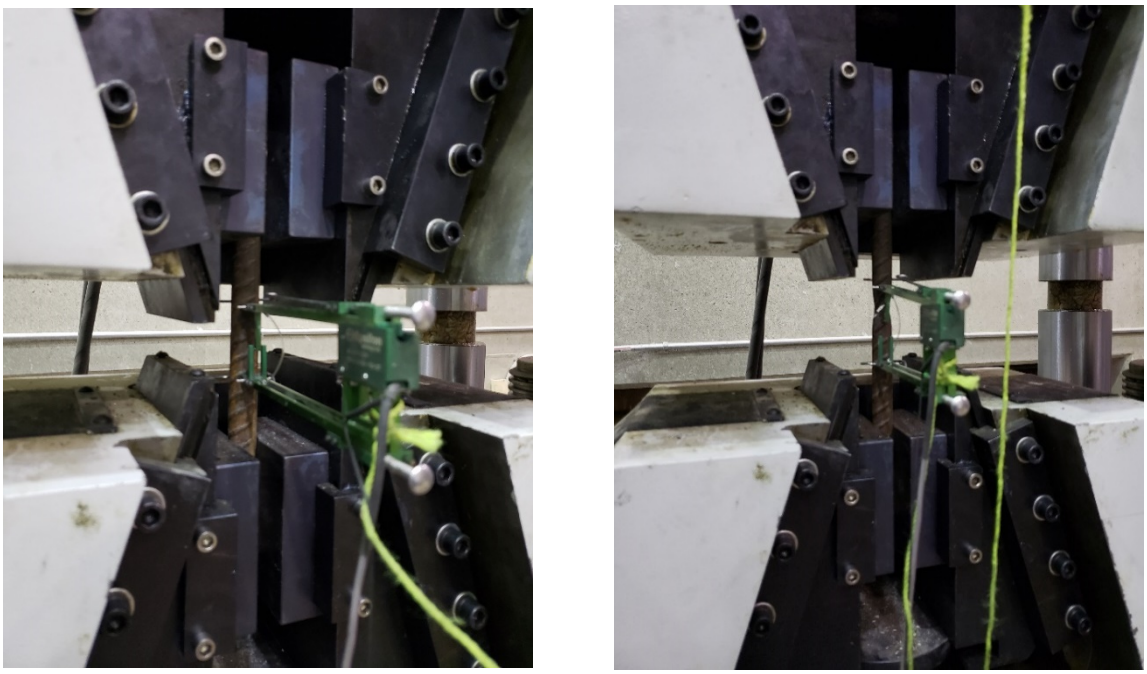

(f) Views of the 20M reinforcing steel coupon # 3 before testing (left) and after failure (right)

(g) Views of the failed reinforcing steel coupons

Figure 3.6 Views of the tensile test setup and the failed reinforcing steel coupons

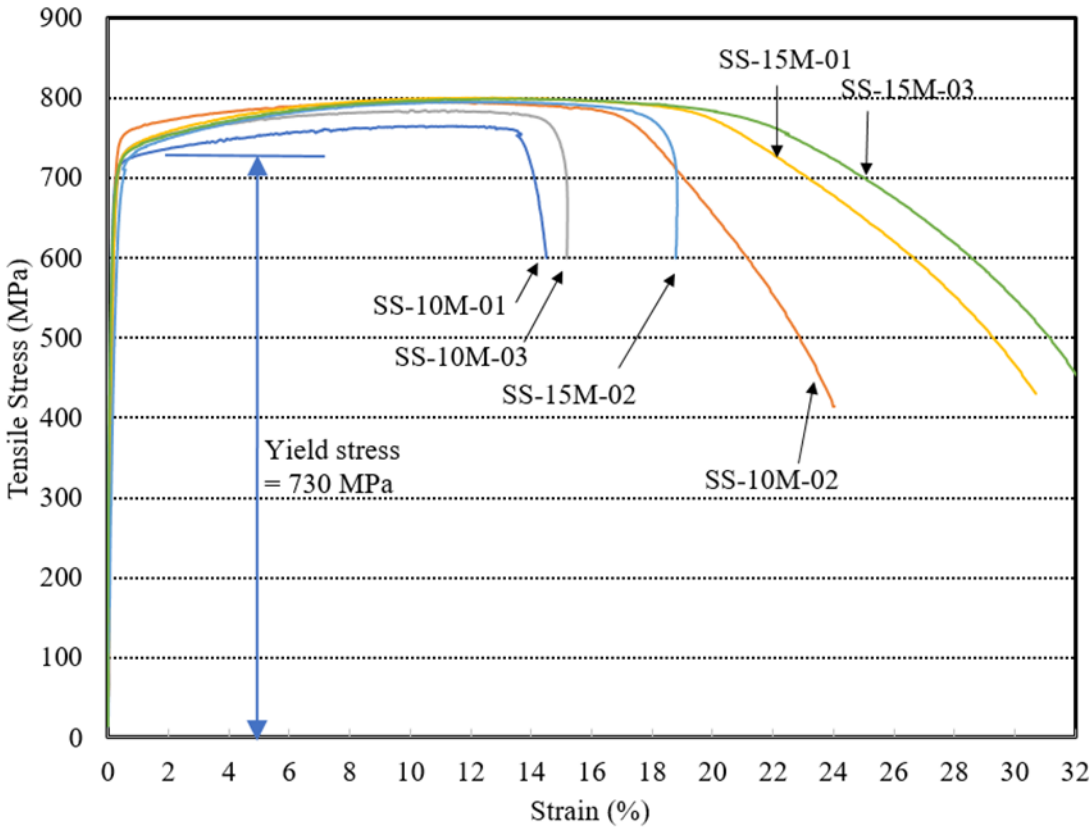

Figure 3.7 Tensile stress-strain relationship for stainless steel bars

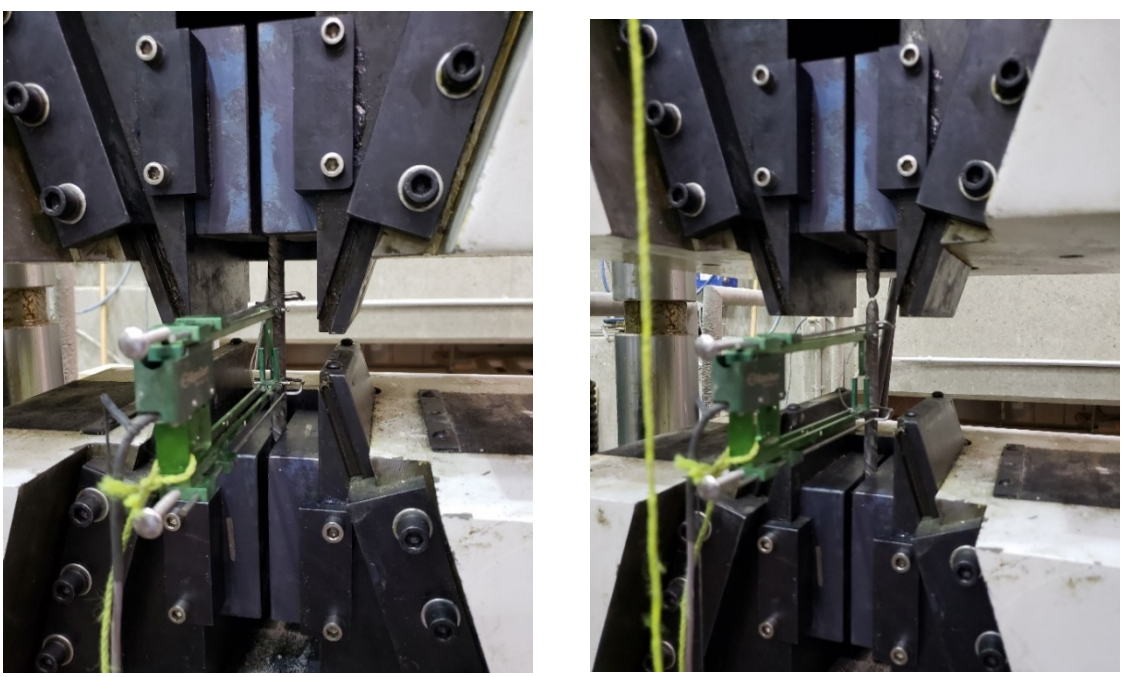

(a) Views of the test setup for 15M stainless steel coupon # 1before testing (left) and after failure (right)

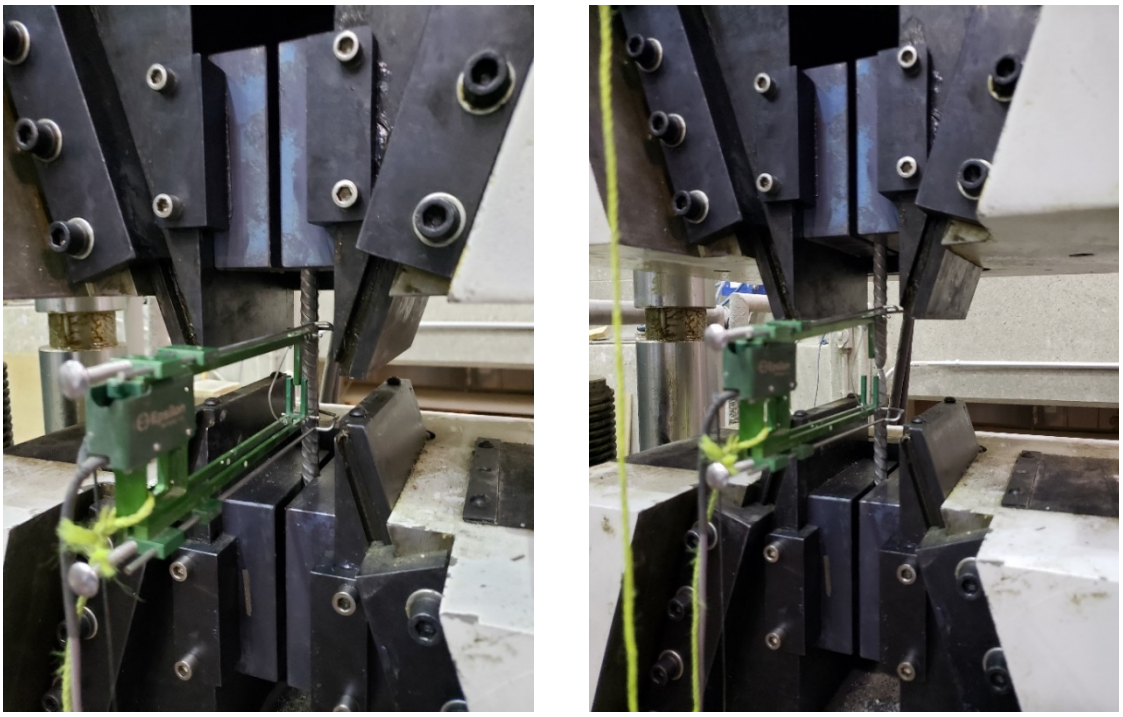

(b) Views of the test setup for 15M stainless steel coupon # 2 before testing (left) and after failure (right)

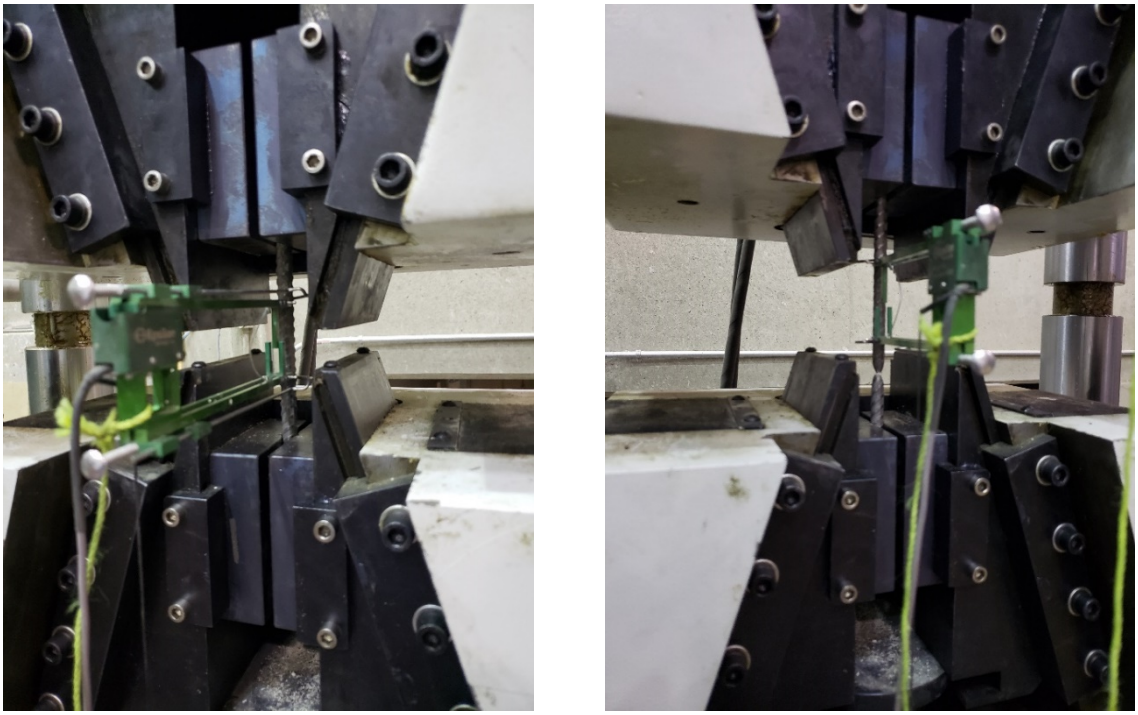

(c) Views of the test setup for 15M stainless steel coupon # 3 before testing (left) and after failure (right)

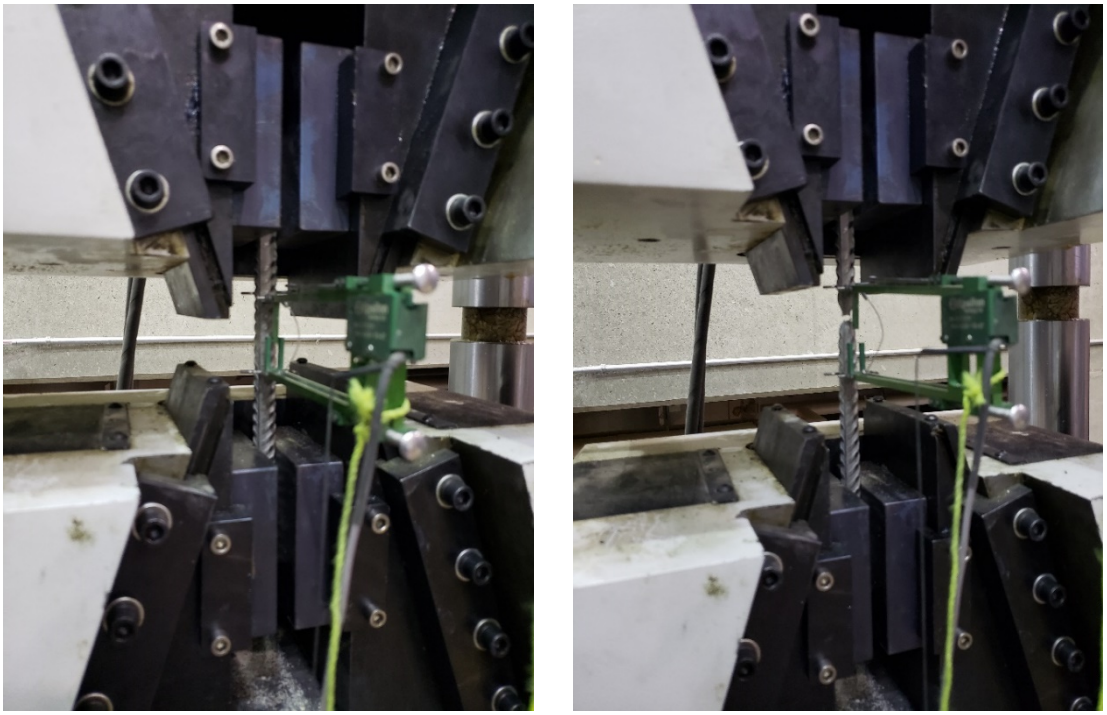

(d) Views of the test setup for 20M stainless steel coupon # 1before testing (left) and after failure (right)

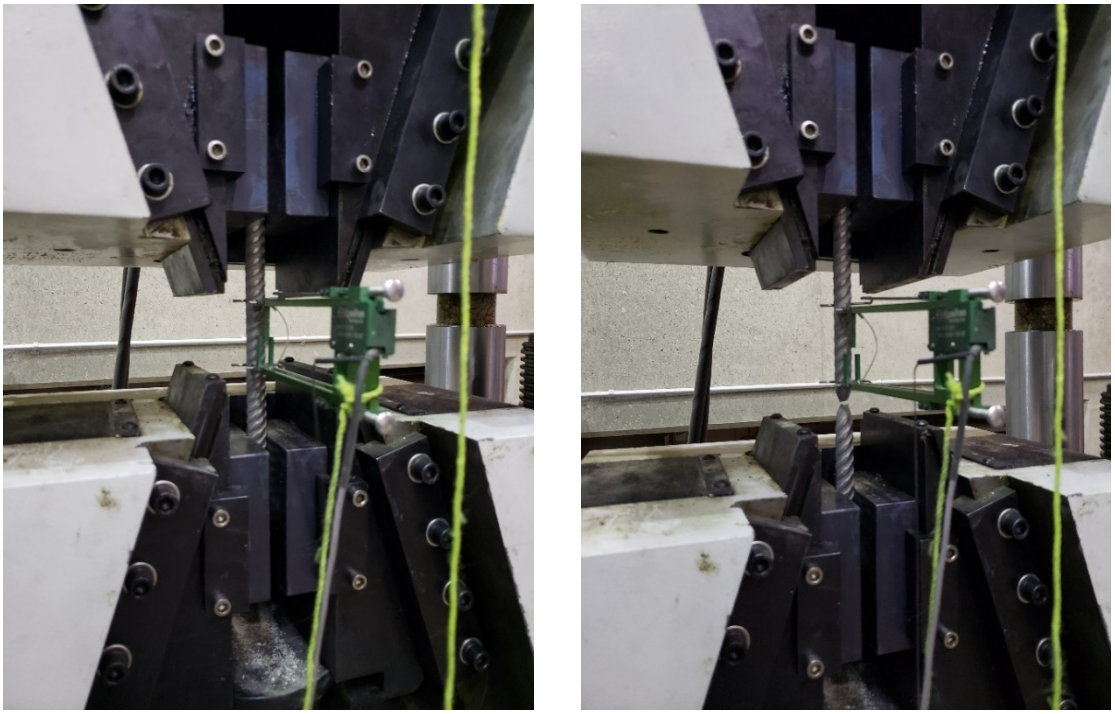

(e) Views of the test setup for 20M stainless steel coupon # 2 before testing (left) and after failure (right)

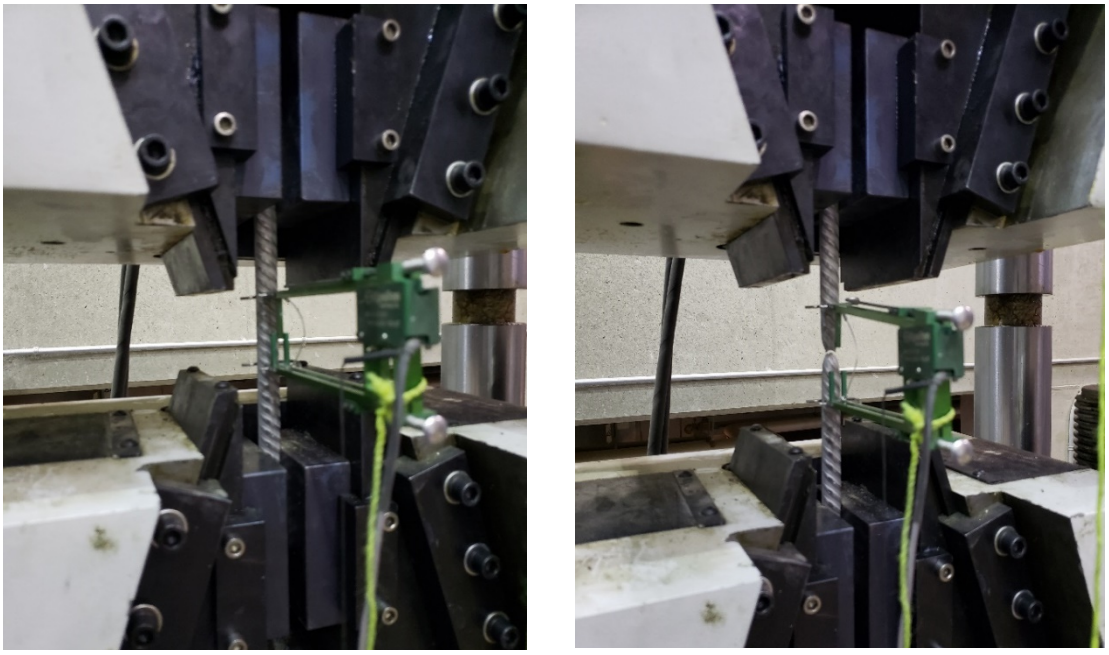

(f) Views of the test setup for 20M stainless steel coupon # 3 before testing (left) and after failure (right)

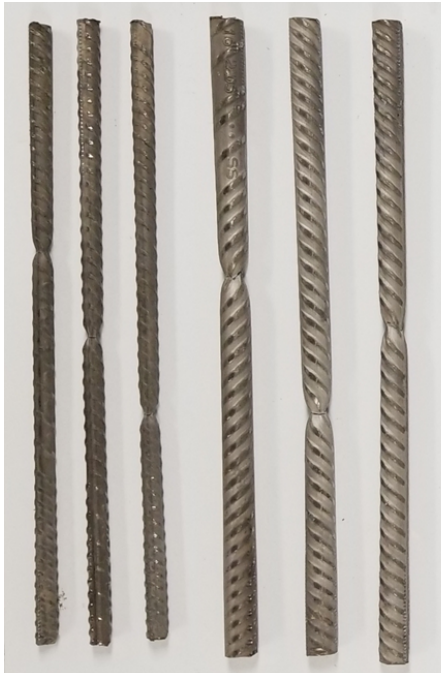

(g) View of the failed stainless-steel coupons

Figure 3.8 Views of the tensile test setup and failed stainless-steel coupons

3.4 Experimental Test Setup and Apparatus

To apply load to the barrier wall, a customized steel loading frame was designed in such a way to be able to support an applied load of up to 1000 kN. The frame consists of an I-Beam supported by two inclined HSS columns as shown in Figure 3.9. All three of these members are welded to steel plates which are anchored into the lab floor. Figure 3.9 shows detailed schematics of the loading frame. Figure 3.10 shows the barrier test setup. The force from the hydraulic jack was applied to the series of I-beams in the loading frame so that the applied load was spread over two trapezoidal wood blocks which were cut to be flush with the barrier wall surface. These pieces of wood are spaced apart in such a way that the overall applied load was distributed over 2.4 m linearly across the barrier wall. The applied load was recorded using a load cell attached to the hydraulic jack. Each barrier specimen was anchored to the lab floor at its rear end as depicted in Figure 10 to eliminate uplift. Also, the base supporting the barrier wall was restraint using steel members as shown in Figure 3.10 to prevent rigid body movement of the barrier base during the test. Specifically, the barrier was anchored using evenly spaced anchor rods across the front end of the slab at three locations, the two ends and the middle point of the slab.

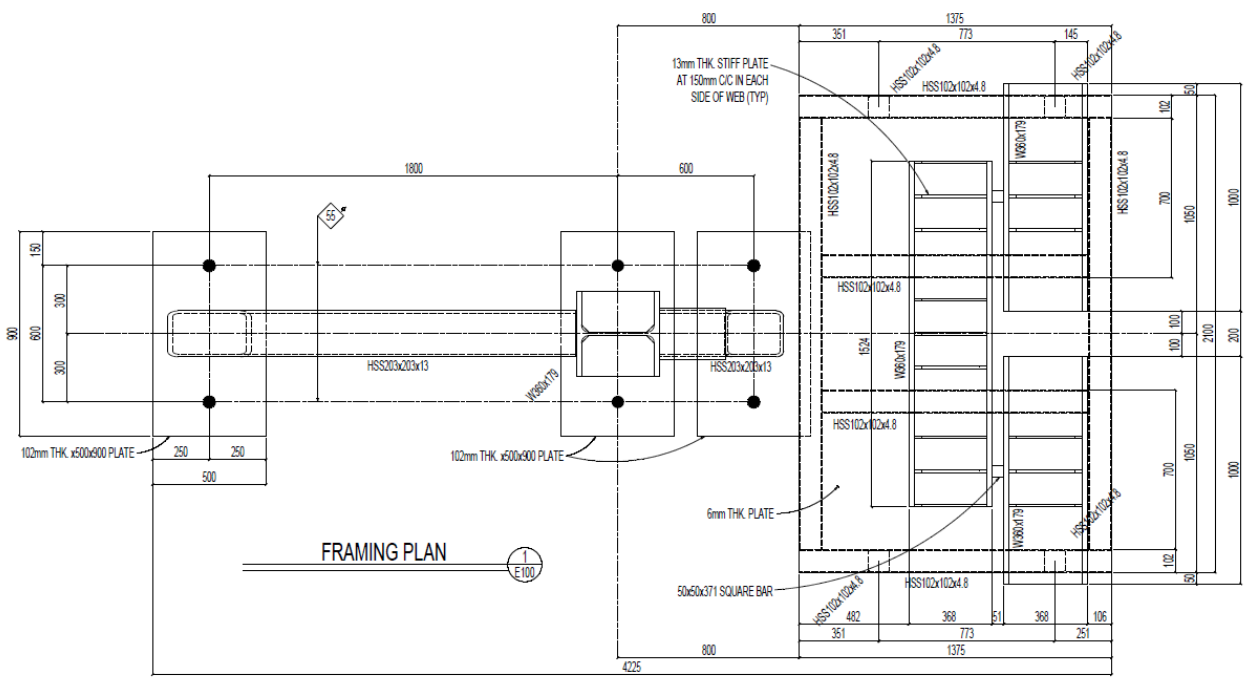

(a) Plan

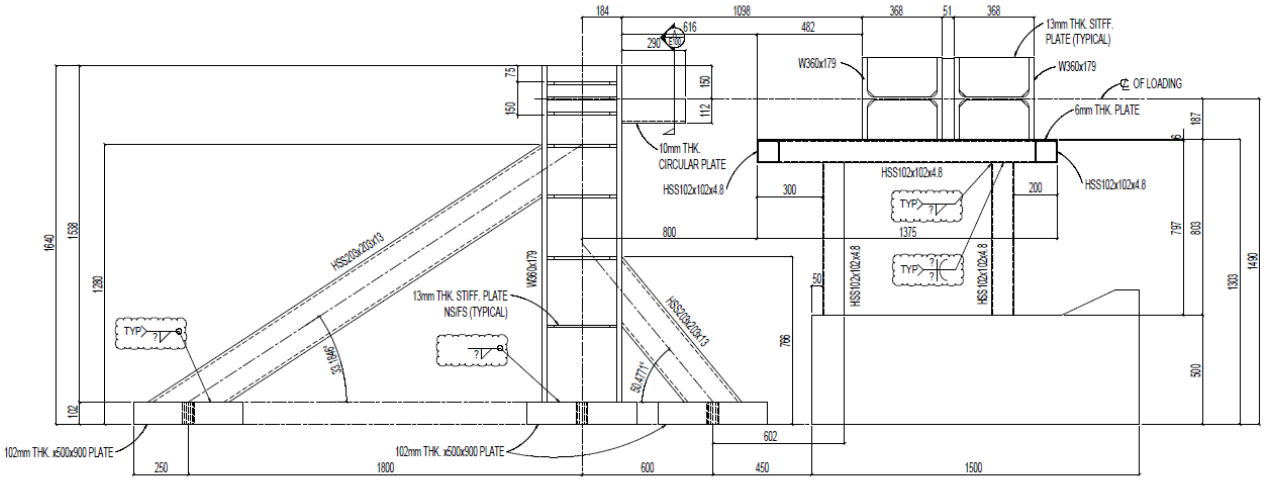

(b) Elevation

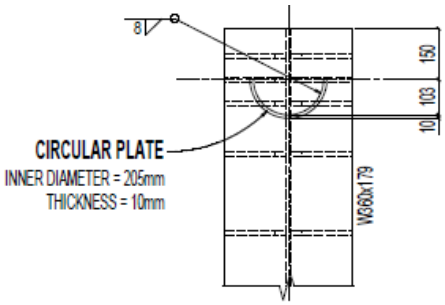

(c) Section A-A

Figure 3.9 Details of the loading frame

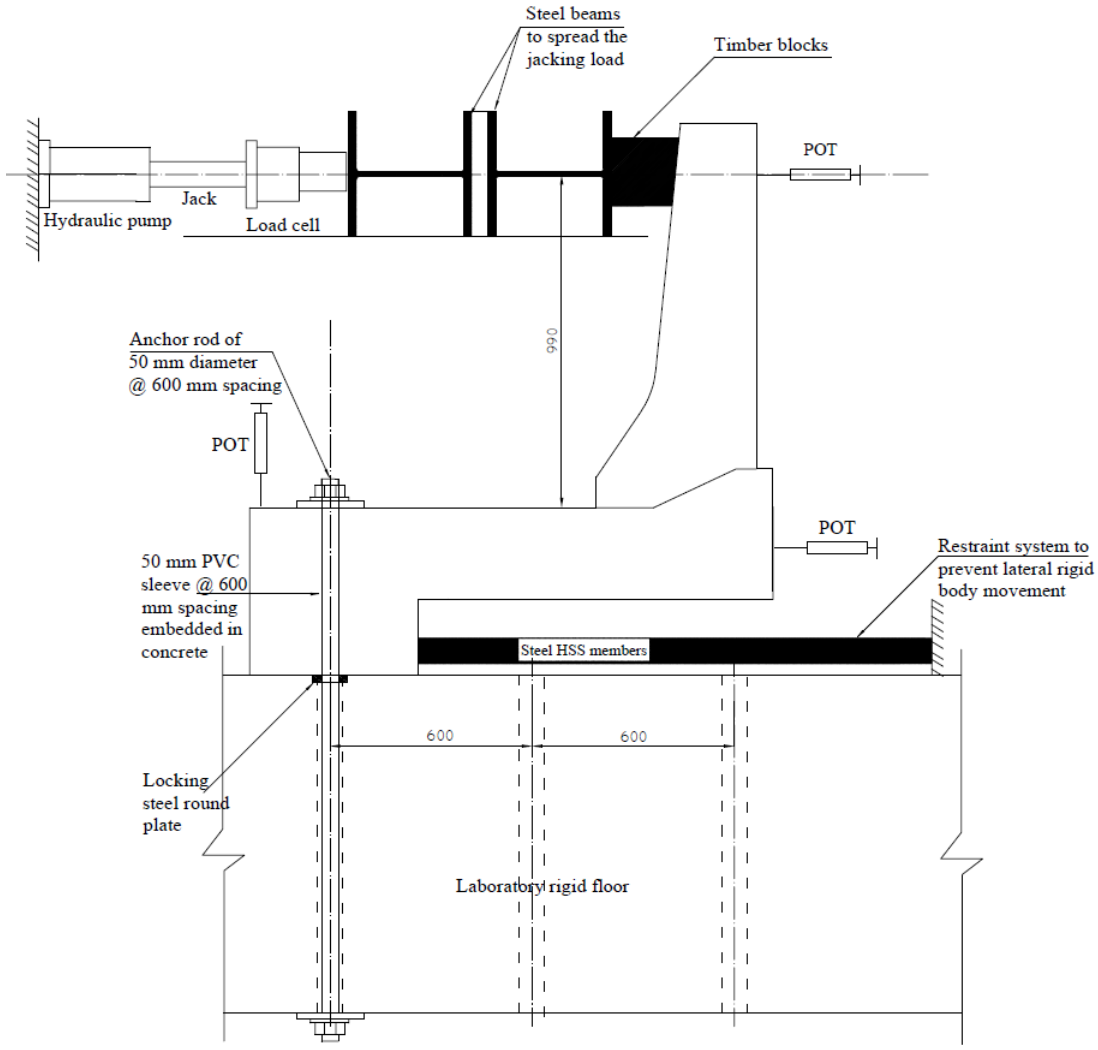

Figure 3.10 Experimental test setup

3.5 Barrier Data Acquisition and Sensor Layout

Figures 3.11 and 3.12 show the arrangement of the vertical reinforcement in the traffic side of the barrier walls of 6.5 m and 4.5 m long, respectively. It should be noted that MTO standard drawing specifies double such front vertical reinforcement at barrier ends. Each barrier specimen was instrumented with potentiometers (POT's/LVDT's) to measure horizontal and vertical displacement of the barrier. Figure 3.13, 3.14, 3.15 and 3.16 show locations of potentiometers in specimens S-1, S-2, S-3 and S-4, respectively.

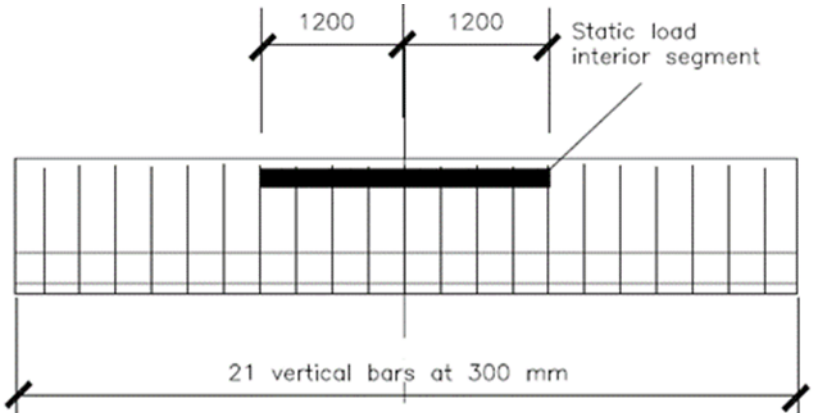

Figure 3.11 Elevation of front vertical reinforcement arrangement for barrier specimens S-3 and S-4 with interior loading

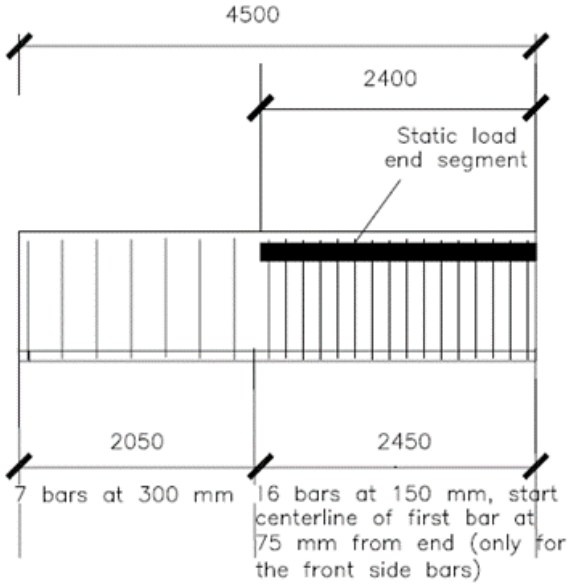

Figure 3.12 Elevation of front vertical reinforcement arrangement for barrier specimens S-1 and S-2 with end loading

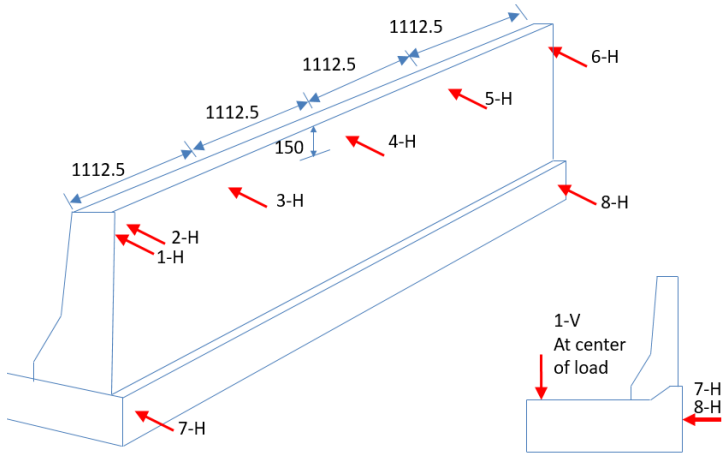

Figure 3.13 Arrangement of potentiometers (LVDTs and POTs) in specimen S-1

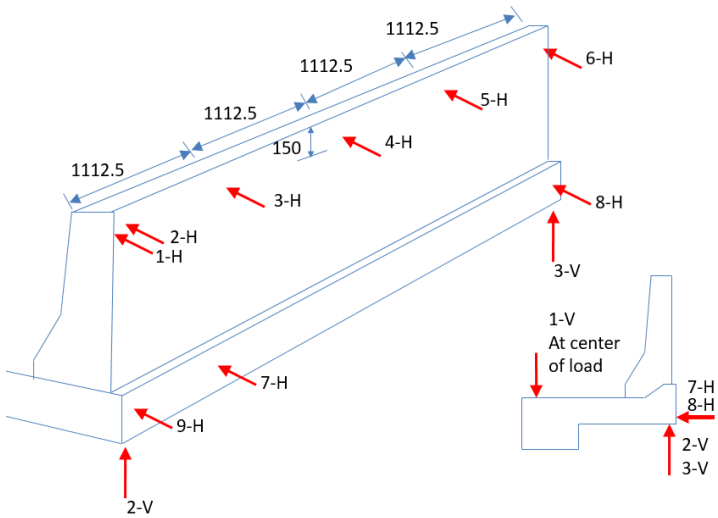

Figure 3.14 Arrangement of potentiometers (LVDTs and POTs) in specimen S-2

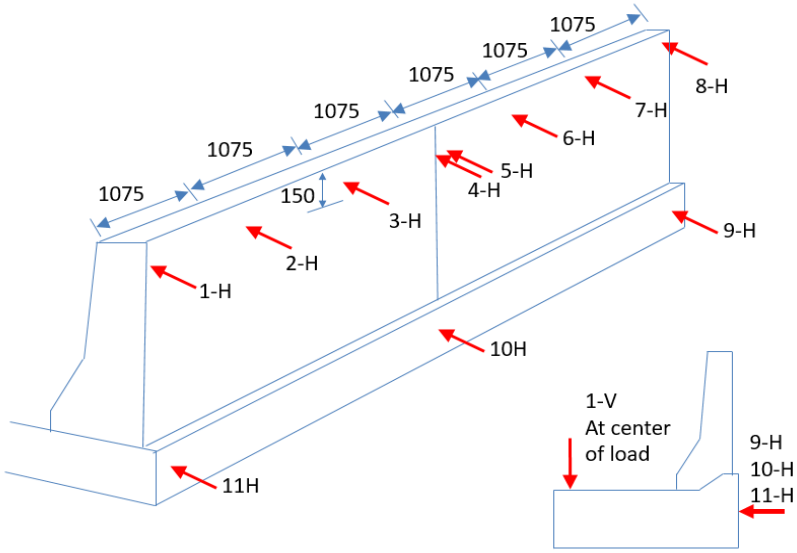

Figure 3.15 Arrangement of potentiometers (POTs) in specimen S-3

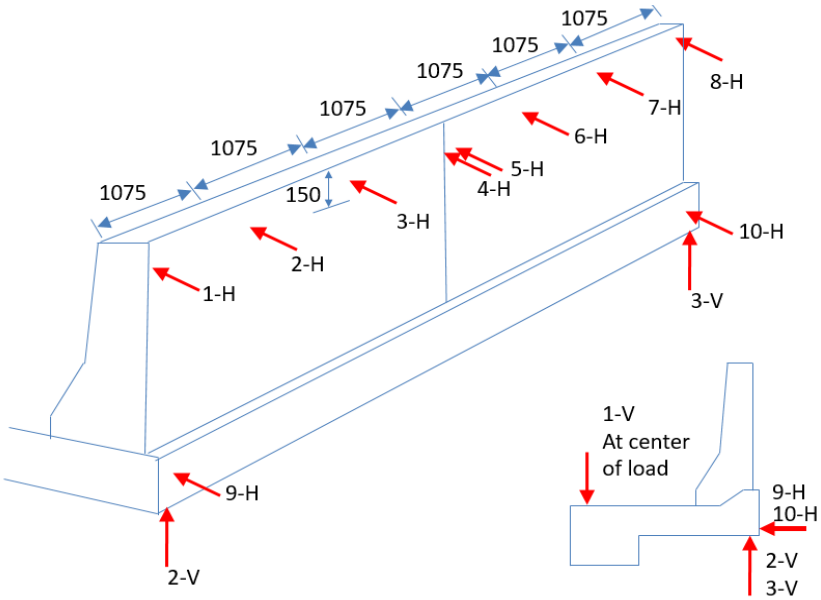

Figure 3.16 Arrangement of potentiometers (POTs) in specimen S-4

3.6 Barrier Construction Process

The following subsections will discuss the process of constructing each segment of the barrier. Figure 3.17, 3.18, 3.19 and 3.20 show photos of specimens S-1, S-2, S-3 and S-4, respectively, during construction.

3.6.1 Construction of Barrier Base

The first stage to constructing the barrier consisted of laying out a tarp over the concrete lab floor, which would act as the base surface for the barrier. Four pieces of plywood were then put together to form the rectangular base of the barrier, reinforced with 2x4 studs at sufficient distances apart. In the case of the specimens with deck slab cantilevers, rectangular foam sections were placed within the wooden formwork across the entire barrier length to create a cantilevered shape upon casting. The wooden formwork was then reinforced with two layers of 2x4 belts to ensure the formwork would not open from the pressure created from the concrete during casting. Finally, the rebar for the base was placed within the formwork according to design, along with equally spaced PVC tubes which serve as the voids in the barrier slab to pass the anchor rods through into the existing lab floor. Pieces of construction yarn were also put across the slab to ensure the proper height of the base (500 mm) during casting.

3.6.2 Construction of Barrier Wall

After the base was cast, the stainless-steel wall reinforcement was placed according to design. It should be noted that the base was properly cured for seven days in parallel to constructing the barrier wall. Once the wall reinforcement was completed, steel forms were put into place for casting of the wall segment of the barrier. The forms were braced and sealed appropriately to ensure no movement of the formwork or leakage occurred during casting.

3.6.3 Barrier Set-up for Testing

Once the concrete was set, the forms were removed to properly cure the entire wall segment of the barrier. To ensure ease of crack visibility during testing, the entire barrier was painted white. A wooden frame was then constructed and placed behind the barrier wall to mount the displacement sensors. Once all the sensors were finalized, all gauges were connected to the data acquisition system. Figure 3.21, 3.22, 3.23 and 3.24 show locations of potentiometers in specimens S-1, S-2, S-3 and S-4, respectively.

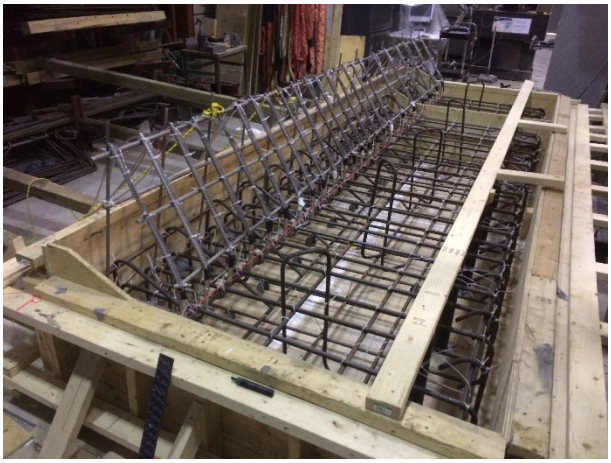

a) Reinforcement before casting the base

b) Reinforcement during casting the base

c) Stainless steel bars after casting the base

d) Side view of barrier reinforcement

e) Elevation of barrier reinforcement

f) Steel form to cast the barrier wall

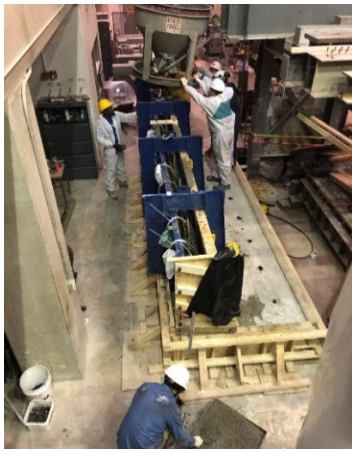

g) Casting the barrier wall

(h) Painting the barrier with white color

Figure 3.17 Sequence of construction of barrier specimen S-1

a) Reinforcement before casting the base

b) Casting of concrete base

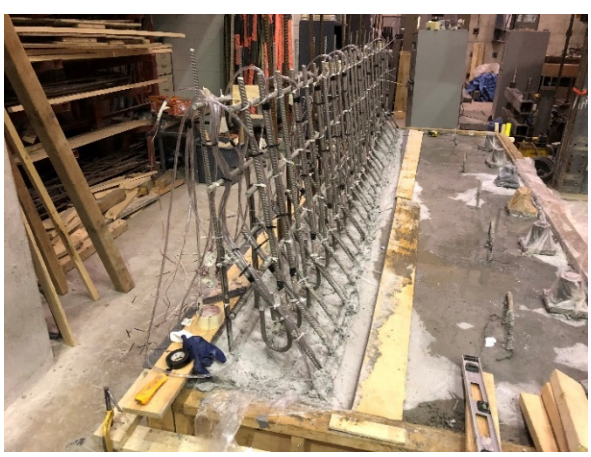

c) Side view of wall reinforcement

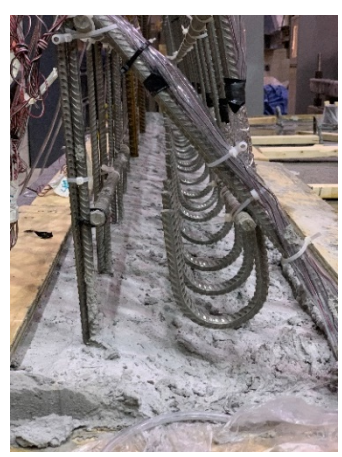

d) Close-up view of wall reinforcement

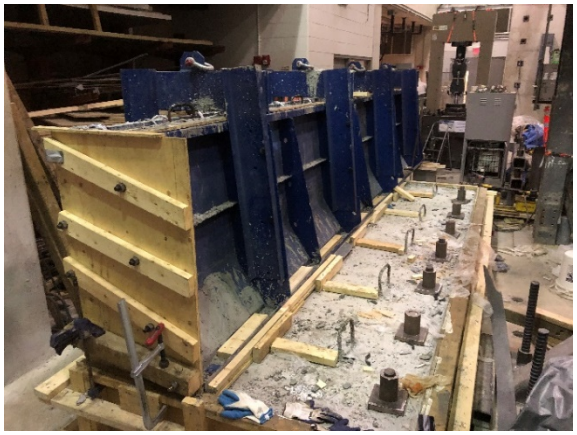

e) Steel form for casting the wall

f) Barrier and base after removing the steel form

Figure 3.18 Sequence of construction of barrier specimen S-2

a) Reinforcement before base casting

b) Wall reinforcement

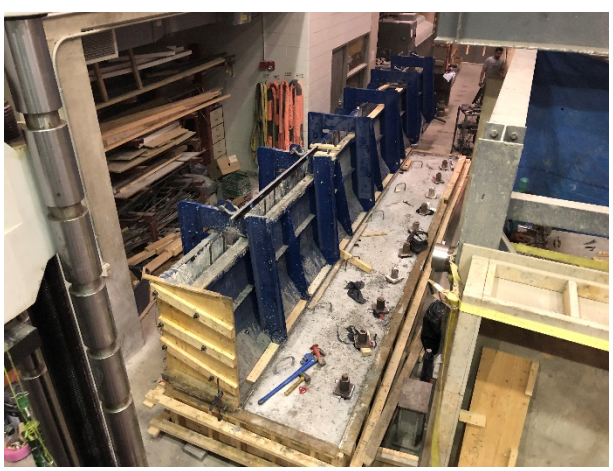

c) Steel form to cast the barrier wall

d) Painting the barrier with while color

Figure 3.19 Sequence of construction of barrier specimen S-3

a) Reinforcement before casting the base

b) Wall reinforcement

c) Steel form to cast the barrier wall

d) Barrier specimen after steel form removal

Figure 3.20 Sequence of construction of barrier specimen S-4

a) Side view of loading frame

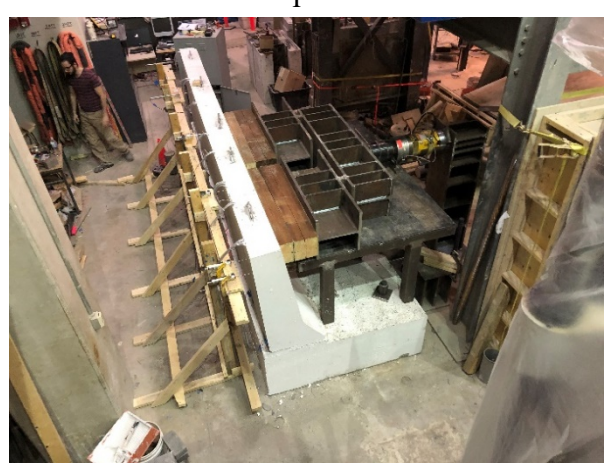

b) Top view of the barrier and loading system

c) Back view of the barrier wall

d) Front view of the barrier wall

Figure 3.21 View of test setup for barrier specimen S-1

a) Side view of loading frame

b) Top view of the barrier and loading system

c) Close-up view of the loading table

d) Side view of the loaded barrier

Figure 3.22 View of test setup for barrier specimen S-2

a) Side view of the loaded barrier wall

b) Lateral restraint to the barrier base

c) General view of the loaded barrier system

d) Back timber frame to support sensors

Figure 3.23 View of test setup for barrier specimen S-3

a) Side view of loading frame

b) Barrier wall and loading system

c) Back timber frame to support sensors

d) Close-up view of top POTs and Pi gauges

Figure 3.24 View of test setup for barrier specimen S-4

Chapter IV

Experimental Results and Discussion

4.1 General

The experimental program included testing four actual-size barriers, two of 6.5 m length and two of 4.5 m length. One barrier in each group was cast over a thick undeformable concrete base, while the other barrier was cast over a short slab cantilever. The 6.5 m long barriers were tested under a transverse line load centered at their mid-length, while the 4.5 m long barriers were tested under exterior line loading. The transverse line loading over 2.4 m length was applied in increments of 25 kN until failure to allow for time to mark crack initiations and propagations. The specimen is considered failed when the applied load could not be increased any further while the deflection continues to increase. At each load increment, the barrier deck and wall were inspected for formation and propagation of cracks. Each crack was marked and labeled with the load it occurred at. Table 4.1 shows a summary of the experimental results for each barrier. The capacity/demand ration in Table 4.1 represents the ratio between the experimental failure load and the CHBDC design load of 357 kN. The following subsections provide discussion of the experimental results for each of the tested specimens.

Table 4.1 Summary of experimental results

Specimen #	**Load location**	**First crack (kN)**	**Failure load (kN)**	**Max. wall deflection (mm)**	**Capacity/ Demand* ratio**	**Failure mode**
S-1	Left end	200	475	19	1.33	Punching shear
S-2	Left end	100	403	40	1.13	Flexure and bar anchorage in slab
S-3	Middle	250	421	9	1.18	Punching shear
S-4	Middle	125	360	27	1.00	Punching shear

* 357 kN factored design transverse loading (CSA, 2019).

4.2 Experimental Results and Discussion for Specimen S-1

Figures 4.1 and 4.2 show photos of cracks in specimen S-1 after failure but before and after the removal of the loading frame and the timber frame supporting the potentiometers, respectively. When analyzing the structural behavior of specimen S-1, it was observed that the first flexural crack occurred at 85 kN at the deck-barrier junction. This crack propagated through the barrier wall thickness as well as in the longitudinal direction of the barrier wall at a load of 200 kN. This horizontal crack propagated diagonally in the barrier wall from a distance of 0.77 m from the barrier end at a load of 300 kN and reached the top of the barrier wall at 300 kN applied load as depicted in Figure 4.2(i). Also, the horizontal crack at the barrier-deck joint propagated further in the longitudinal direction of the barrier wall, and then extended diagonally in the barrier wall at 350 kN and 375 kN from at distances of 1.53 m and 2.15 m from the barrier end, respectively. These two diagonal cracks reached the top of the barrier wall at a load of 300 kN, and 400 kN, respectively. Similar horizontal cracks appeared at the intersection of the two tapered portions of the barrier wall at 250 kN applied load and propagated horizontally over a length of 1.53 m before extending diagonally towards the top of the barrier wall. Other horizontal cracks appeared in the top tapered portion of the barrier wall with increase of applied load beyond 250 kN. Once the diagonal cracks reached the top of the barrier wall, they propagated through the thickness of the barrier towards its back side with increase in applied load until sudden punching shear failure occurred just at the end of the timber block used to apply the line load on the barrier wall at 475 kN. At this time, the jacking load continued to be applied to expand the punching shear zone to the end of the barrier wall but with no apparent increase in the applied load. After testing, the barrier wall was saw cut at 1 m from its end as depicted in Figure 4.3. Such a saw-cut showed the diagonal punching shear crack at 38°.

At the back of the barrier wall, a few vertical and diagonal cracks appeared at 325 kN and propagated towards the base of the barrier with load increase as depicted in Figures 4.2(d) through 4.3(f). Figure 4.2(a) showed signs of anchorage cracks at the bottom end of the stainless-steel bent bars in the deck slab at a load of 400 kN and propagated further with increase of applied load until a punching shear crack occurred at the top of the barrier wall. The recorded ultimate failure load of 475 kN is greater than the CHBDC factored design transverse loading of 357 kN, leading to a capacity-demand ratio (CDR) of 1.33. Figure 4.4 shows the load-deflection relationship for

specimen S-1. One may observe the nonlinear behavior of the specimen beyond the cracking load. At the failure load, the maximum recorded deflection at the loaded end of the barrier was 19 mm, while the maximum deflection at the unloaded end was -0.25 mm. The recorded barrier uplift at the location of the tie-down system was 0.07 mm at the failure load which is considered negligible.

When looking at the overall flexural crack pattern of this barrier, it can be seen that a trapezoidal crack pattern is exhibited in contrast to the AASHTO-LRFD triangular yield line pattern.

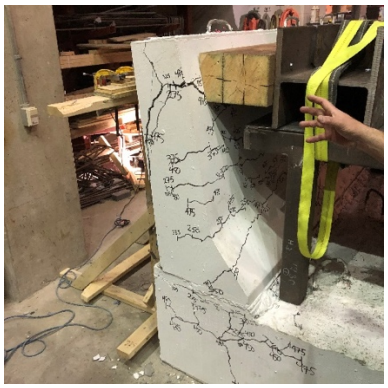

a) Flexural cracks in barrier wall and anchorage cracks in the concrete base

b) Propagation of horizontal cracks with the loaded length that propagated diagonally towards the unloaded barrier portion

c) Punching shear crack at internal end of the patch loading

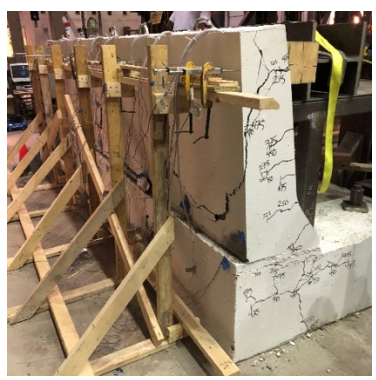

d) Propagation of the punching shear plane along the patch loading length

Figure 4.1 Views of crack pattern and failure mode for specimen S-1 before removing the testing frame

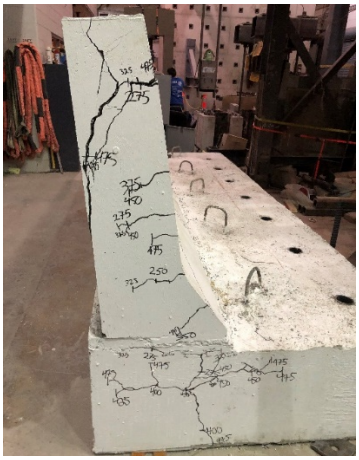

a) Flexural cracks in the wall and bar anchorage cracks in the base

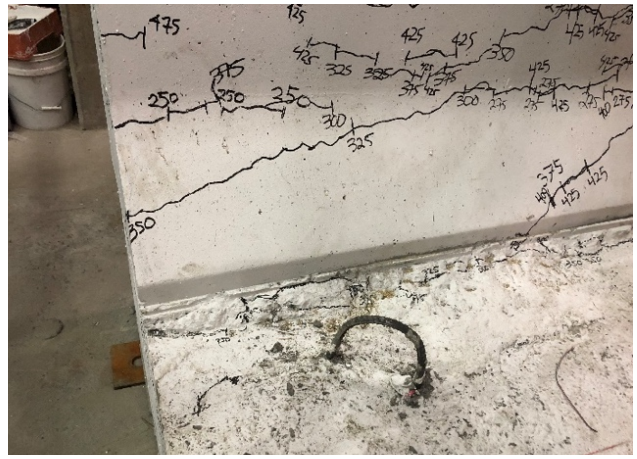

b) Horizontal flexural crack in the barrier wall and along barrier-base interface

c) General view of final crack pattern

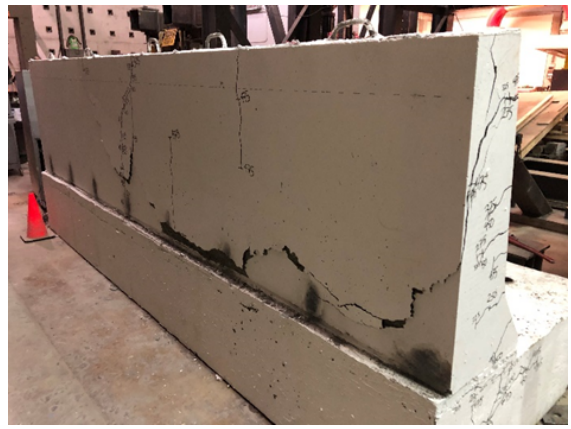

d) Propagation of the punching shear plane along the loaded length

e) Punching shear at end of loaded length

f) Vertical crack at back face at 1.8 m from the barrier's south end

g) Top view of punching shear through barrier thickness

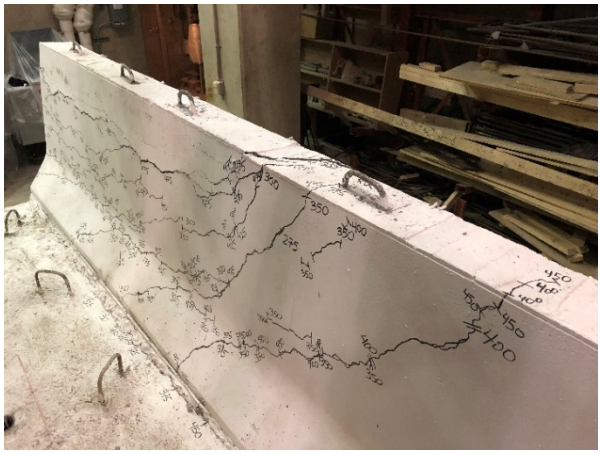

h) Side view of punching shear failure

i) Crack pattern at failure

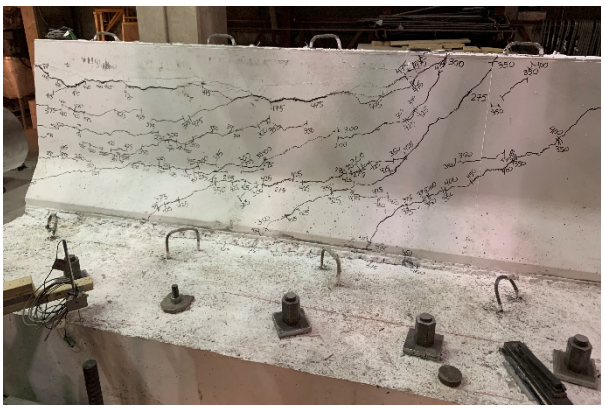

j) Close-up view of flexural cracks in the wall

Figure 4.2 Views of crack pattern and failure mode for specimen S-1 after removing the testing frame

Figure 4.3 Saw cut at center of 1 m from the south end of barrier specimen S-1, looking north, showing 38° angle of punching shear failure

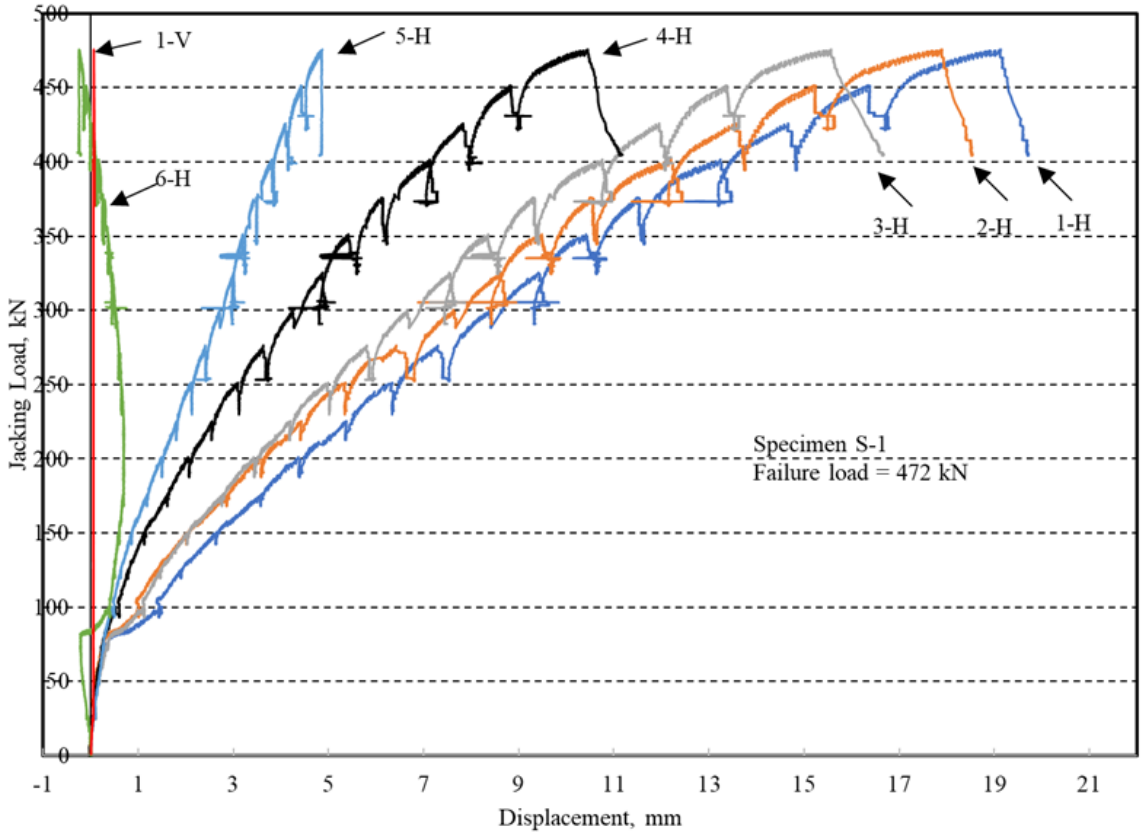

Figure 4.4 Load-deflection relationship of specimen S-1

4.3 Experimental Results and Discussion for Specimen S-2

Figures 4.5 and 4.6 show photos of cracks in specimen S-2 after failure but before and after the removal of the loading frame and the timber frame supporting the potentiometers, respectively. When analyzing the behavior of specimen S-2, it was observed that the first flexural crack occurred at 45 kN from the load-deflection relationship in Figure 4.8, while the first visible flexural crack occurred in the deck slab at the traffic side of the barrier wall at 100 kN with a similar crack occurred at the fixed end of the cantilever slab at 150 kN as depicted in Figures 4.6(b) and (c). Similar flexural cracks appeared in the deck slab cantilever at the unloaded end of the barrier wall at an applied load of 200 kN as depicted in Figure 4.6(f). These flexural cracks at the loaded end of the barrier propagated towards the other side and through the slab thickness with increase of applied load as depicted in Figure 4.6(c). Similar observation was noted at the unloaded end of the barrier wall as depicted in Figure 4.6(f). This observation confirms that the 4.5 m long cantilever behaves in flexure along its entire length. Figure 4.6(g) shows a few flexural cracks at the intersection of the two tapered portions of the barrier wall as well as within the top tapered portion starting from 250 kN applied load. However, the horizontal crack at the barrier deck joint extended diagonally into 3 flexural cracks at 350 kN, 375 kN and 400 kN applied load from distances of 2 m, 2.3 m and 2.7 m from the loaded end of the barrier wall as depicted in Figure 4.6(h). These horizontal and diagonal cracks in the barrier wall were not significant to case failure. However, the first diagonal crack propagated through the thickness at the top of the barrier wall and extended to the back side of the barrier wall at failure in a form similar pattern to the punching shear crack as depicted in Figure 4.6(j). However, excessive anchorage cracks were noticed at the bottom end of the stainless-steel bent bars embedded in the deck slab as shown in Figures 4.6(b) and 4.6(f) at the loaded end and unloaded end of the barrier wall, respectively, leading to specimen failure. The barrier wall was sawcut at its mid-length to observe the anchorage cracks at the barrier deck junction which was observed in the saw-cut portion shown in Figure 4.7(a). Figure 4.6 shows 3 diagonal cracks at the back of the barrier wall oriented opposite to the 3 diagonal cracks at the traffic side and initiated at applied loads of 250 kN, 300 kN and 403 kN.

Specimen S-2 did not exhibit a punching shear failure, but instead it failed due to flexure at the interface between the deck and the barrier, as well as excessive anchorage cracks at the bottom end of the stainless-steel bars embedded in the deck slab as depicted in Figure 4.7(a). The ultimate

failure load was recorded as 403 kN which is greater than the CHBDC factored design transverse loading of 357 kN, leading to a capacity-demand ratio (CDR) of 1.13. Figure 4.8 shows the load-deflection relationship for specimen S-2. At the failure load, the maximum recorded deflection at the loaded end of the barrier was 40 mm, while the maximum deflection at the unloaded end was 25 mm. The recorded barrier uplift at the location of the tie-down system was 0.7 mm at the failure load which is considered negligible. The deck slab maximum deflection at the ultimate load was 22 mm and 19 mm at the loaded and unloaded ends of the barrier wall, respectively, which confirmed be considerable bending deformation of the deck slab cantilever and associated failure mode.

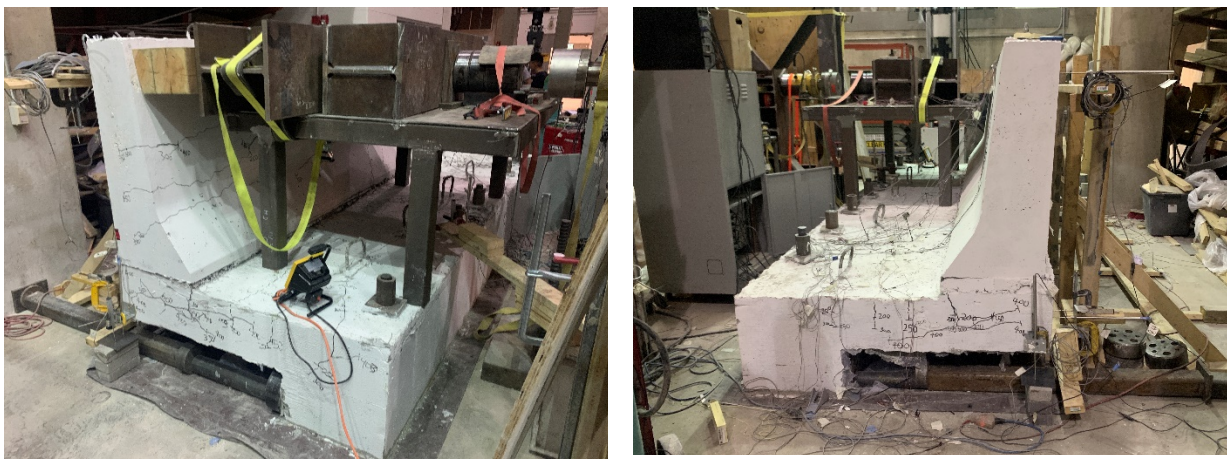

a) South side of the barrier wall

b) North side of the barrier wall

Figure 4.5 Views of crack pattern and failure mode for specimen S-2 before removing the testing frame

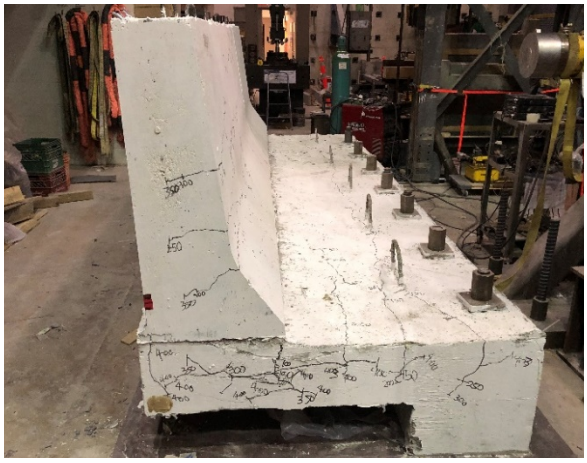

a) Flexural cracks in the barrier wall and deck at the south end

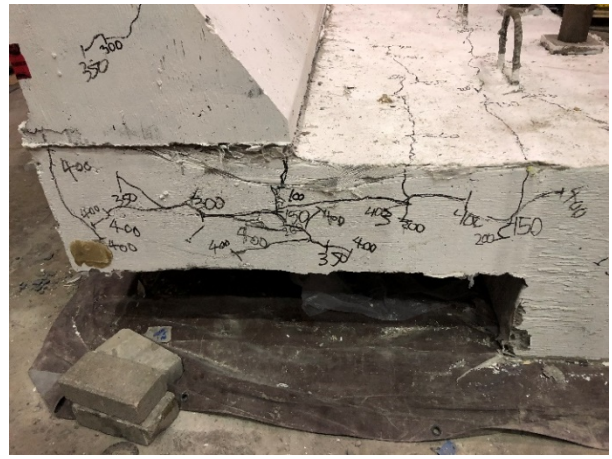

b) Close-up view of flexural cracks and bar anchorage crack in the deck cantilever

c) Flexural crack in deck cantilever

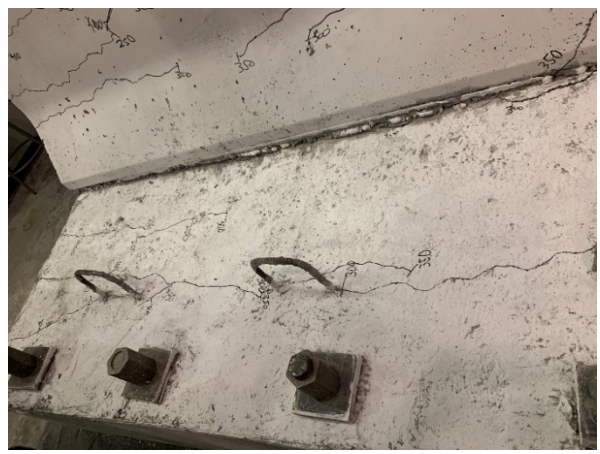

d) Propagation of flexural crack along the length of the deck cantilever

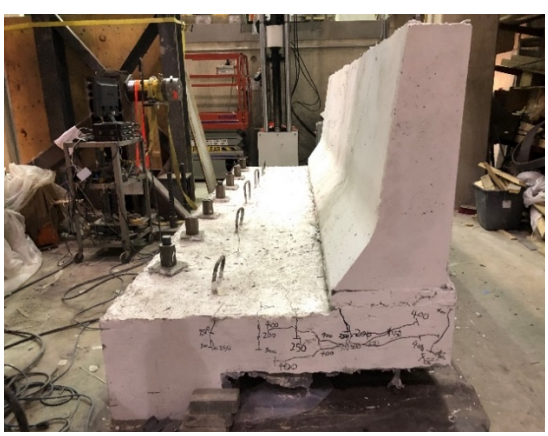

e) Flexural cracks in the barrier wall and deck at the north end

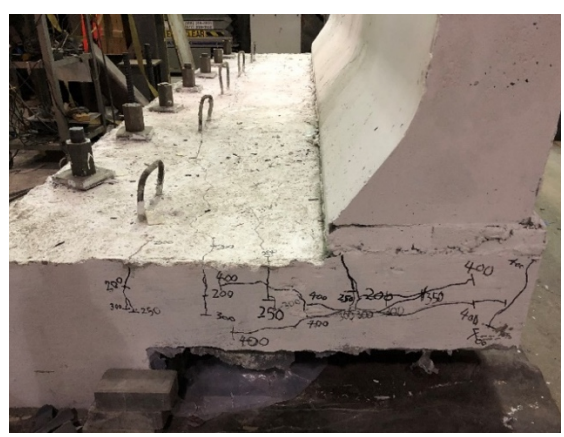

f) Close-up view of flexural cracks and bar anchorage crack in the deck cantilever

g) Flexural cracks in the barrier and deck viewed from the south side

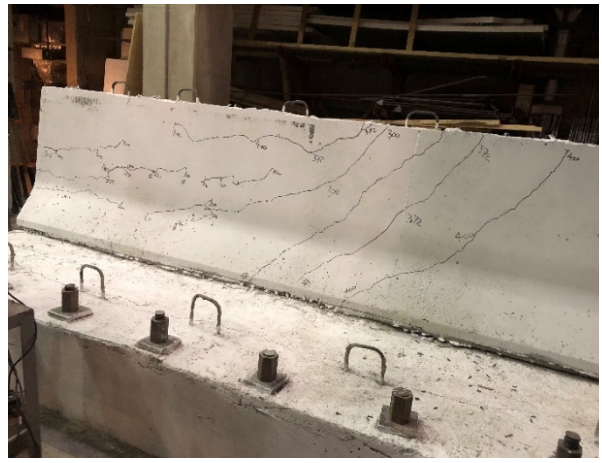

h) Front view of flexural cracks in the wall

i) Crack pattern at back face of barrier showing slightly vertical cracks along the barrier loaded length

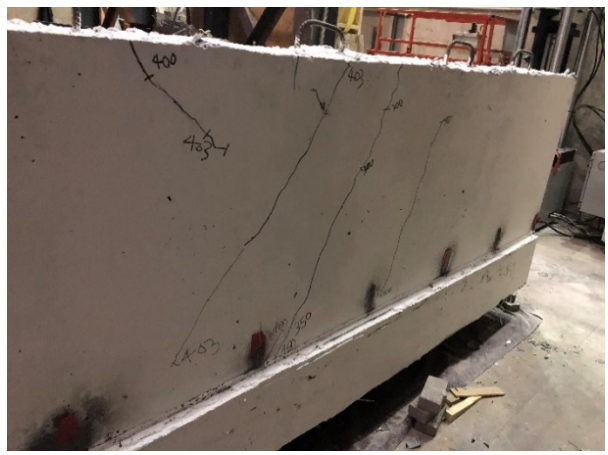

j) Sign of diagonal crack at top of the barrier wall at potential location of punching shear

Figure 4.6 Views of crack pattern and failure mode for specimen S-2 after removing the testing frame frame

a) Saw cut at center of barrier length, looking south, showing flexural crack in the deck, anchorage crack for embedded bent bar in deck, and flexural crack at point of intersection of tapered portions in front side of barrier

b) Saw cut at 1 m away from the center of barrier length in the unloaded portion, looking north, showing flexural crack in the deck and anchorage crack for embedded bent bar in deck

Figure 4.7 Views of crack pattern and failure mode for specimen S-2 after saw-cut

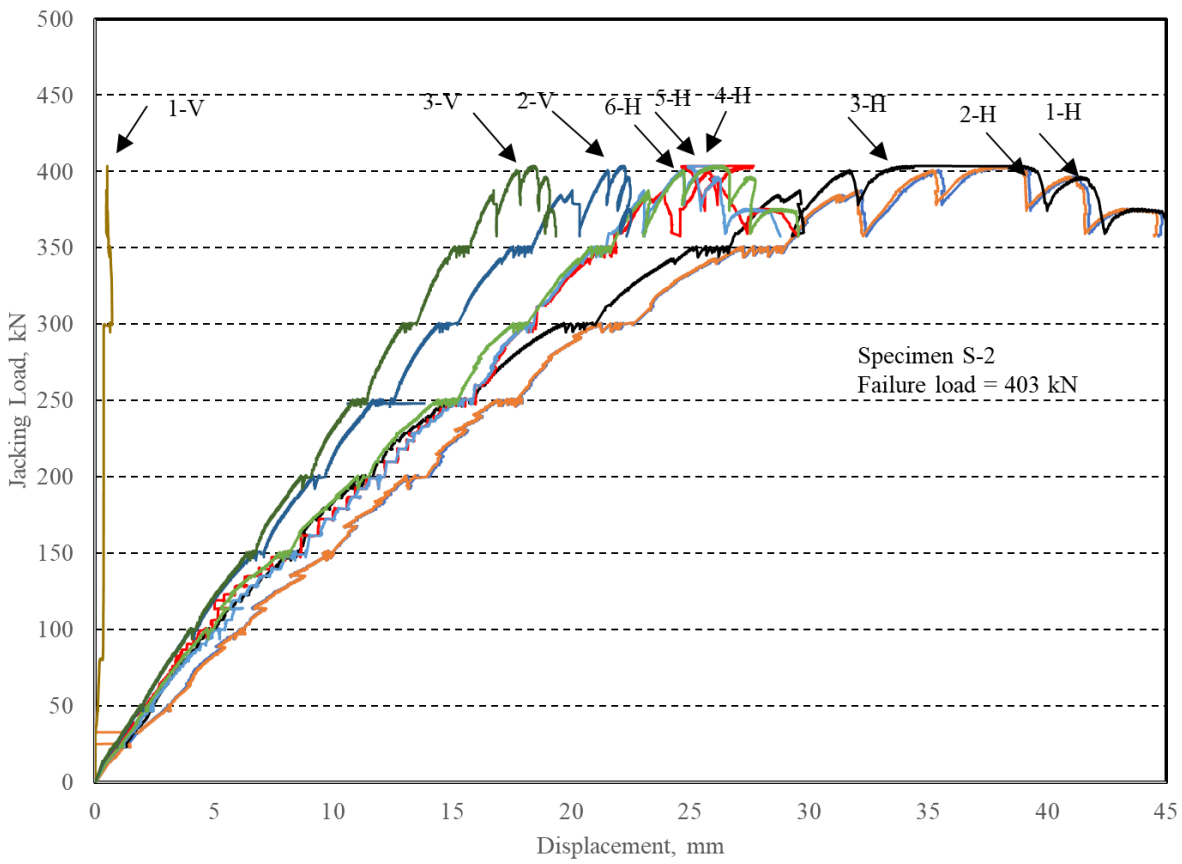

Figure 4.8 Load-deflection relationship for specimen S-2

4.4 Experimental Results and Discussion for Specimen S-3

Figures 4.9 and 4.10 show photos of final cracks in specimen S-3 before and after the removal of the loading frame and the timber frame supporting the potentiometers, respectively. When analyzing the behavior of specimen S-3, it was observed that the first flexural crack occurred at the barrier-deck joint at 120 kN. This horizontal cracks propagated horizontally from the centre of the barrier towards its ends for lengths of 1.55 m and 1.75 m, then extended diagonally in the barrier wall at 350 kN and 300 kN, respectively, as depicted in Figure 4.10(d). Another major horizontal flexural crack appeared at the intersection of the two tapered portions of the barrier front side at 250 kN load and propagated diagonally towards the top of the barrier at the ends of the loaded length at 300 and 350 kN, respectively. Then, a sudden and major punching shear crack occurred at the top of the barrier just on the left side of the loaded length as depicted in Figure 4.10(b). At the same time, a local punching shear crack was observed at the top of the barrier wall between the timber blocks in the loading frame. However, such local punching crack did not propagate further while trying to increase the applied load using the hydraulic jack. On the other hand, a punching shear crack appeared on just at the right side of the loaded length. While trying to increase the applied load, the barrier wall continued to deform to the extent that the punching shear crack to the left and right of the loaded length propagated toward each other to form a complete punching shear crack at the back of the barrier wall as depicted in Figure 4.10(g). After testing, the barrier wall was saw cut vertically between the two timber blocks used to apply the line loading as well as at the right and left ends of the loaded length. Figure 4.11 depicts the punching shear crack at each location with an average angle of 40°.

In the right photo in Figure 4.11(b), one may notice the top local crack that appeared locally during testing along with the final punching shear crack under it, is a result of the global punching shear failure of the specimen. The appearance of the local punching shear crack between the timber blocks may be attributed to the fact that the loading system had a main steel beam connected to two spread steel beams using steel bars welded to each one of them rather than being flexible to allow for spread beam rotation when sudden punching shear occurred at the left side of the loaded length. The ultimate failure load of specimen S-3 of 421 kN is greater than the CHBDC factored design transverse loading of 357 kN, leading to a capacity-demand ratio (CDR) of 1.18. Figure 4.12 shows the load-deflection relationship for specimen S-3. At the failure load, the maximum

recorded deflection at mid-length of the barrier wall was 9 mm, while the maximum deflection at the barrier ends were as 3.7 and 2 mm. The recorded barrier uplift at the location of the tie-down system was 2 mm at the failure load which is considered small. At the back of the barrier wall, Figure 4.11(g) shows that no vertical crack occurred at the centre of the load location which contradicts with the hypothesis of having a vertical crack at this location in the AASHTO-LRFD yield line pattern. One may observe a vertical crack at the back face of the barrier at 1 m from the centre of the barrier length at 250 kN in addition to a diagonal crack originated at the same location at the top of the barrier wall and propagated towards the slab base with increase of applied load. A similar diagonal crack is mirrored on the other side of the barrier midpoint by at 1.4 m from the top of the barrier.

a) Horizontal cracks within the loaded length progagated diagonally in the uloaded portion of the barrier wall

b) Punching shear crack at the south end of the loaded length that propagated to the north side of the loaded length

c) Local punching shear crack at top of wall that did not propagate further

d) Punching shear crack at the north end of between the timber blocks in the loading frame loaded length that propaged to the south side of the loaded length

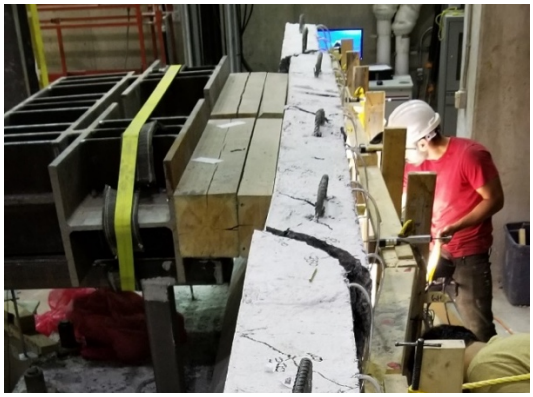

e) Punching shear failure pattern between the beginning and end of the loaded length

Figure 4.9 Views of crack pattern for specimen S-3 before removing the testing frame

a) Front view of flexural cracks within the loaded length

b) Pnching shear crack and flexural cracks extending diagonally in the uloaded portion, looking north

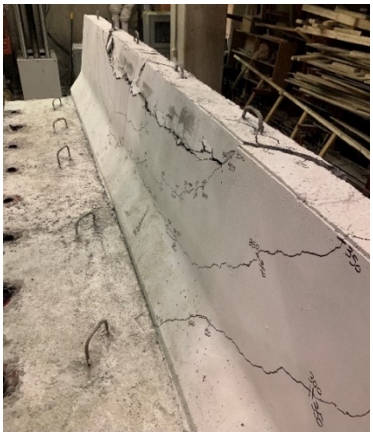

c) Side view of the punching shear failure

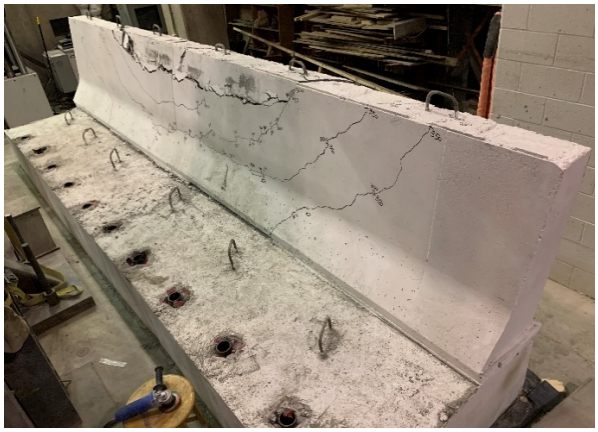

d) Crack pattern looking south

e) Punching shear failure at the south end the of the loaded length

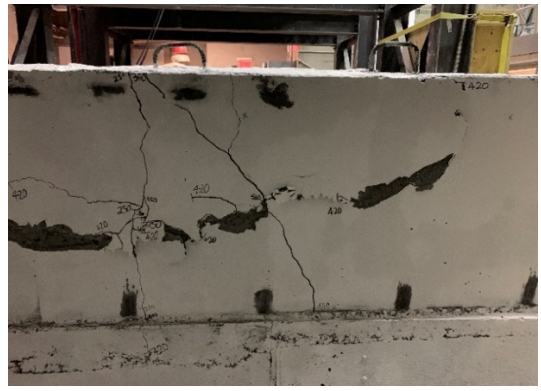

f) Slight vertical cracks at the back face of barrier wall within the loaded length

g) Local punching shear crack at top of wall between the timber blocks that did not propagate further

h) Punching shear crack at the north end of loaded length that propaged to the south side of the loaded length

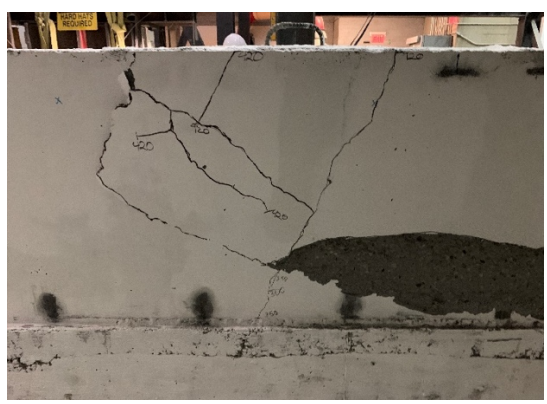

i) Slight vertical cracks at the back face of the barrier wall within its loaded length, close to its north end

Figure 4.10 Views of crack pattern and failure mode for specimen S-3 after removing the testing frame

a) Saw cast at 1 m away from the center of applied load towards the south end showing 40° angle for the punching shear crack

b) Saw cast at 100 mm away from the center of applied load towards the north end showing 40° angle for the global punching shear crack while the local punching shear crack appeared on top of it in the right photo

Figure 4.11 Views of crack pattern and failure mode for specimen S-3 after saw-cut

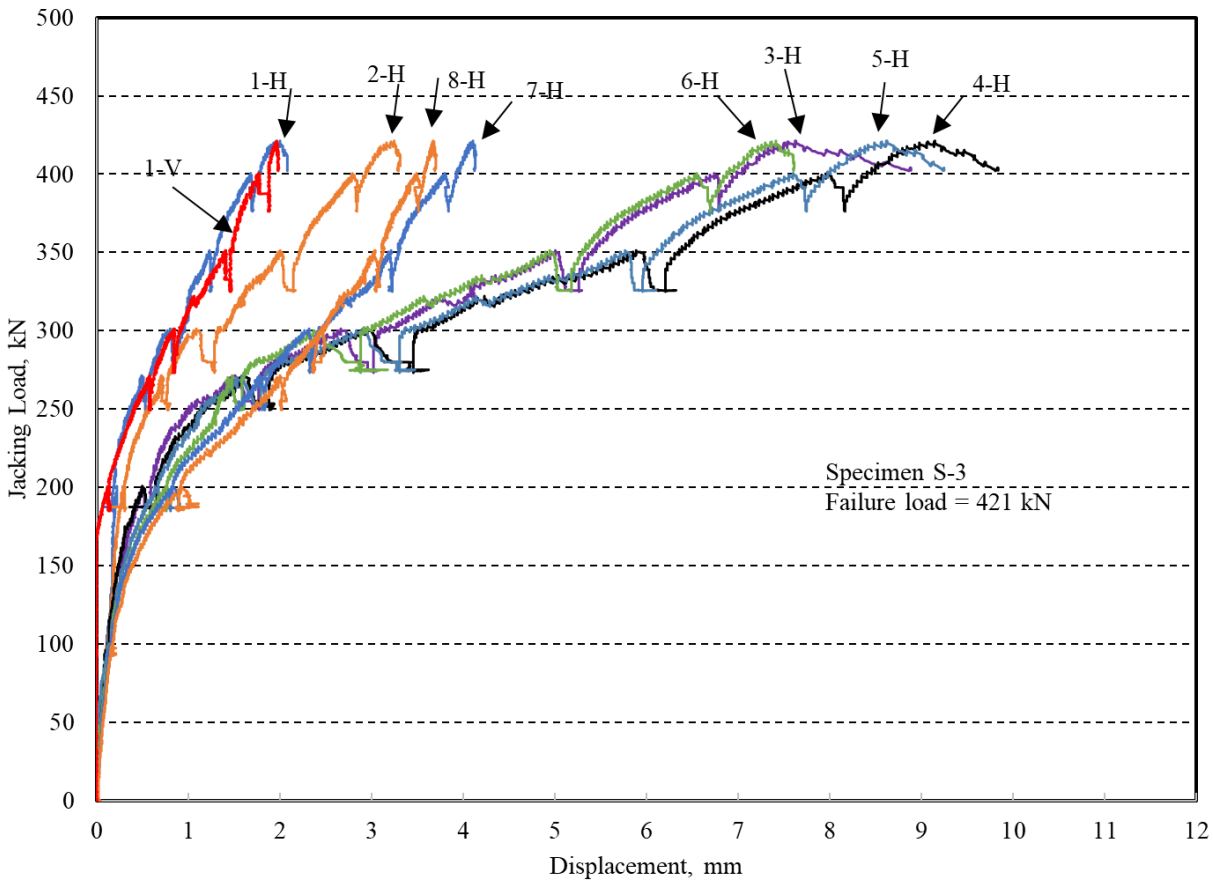

Figure 4.12 Load-deflection relationship for specimen S-3

4.5 Experimental Results and Discussion for Specimen S-4

Figures 4.13 and 4.14 show photos of final cracks in specimen S-4 before and after the removal of the loading frame and the timber frame supporting the potentiometers, respectively. When analyzing the behavior of specimen S-4, it was observed that the first flexural crack occurred at the barrier-deck joint at 125 kN. This horizontal crack propagated horizontally towards the ends of the barrier wall, with one side only extending as a diagonal crack into the lower tapered portion of the barrier wall as depicted in Figure 4.14(f). When comparing this observation with the extensive diagonal cracks in specimen S-3, one may conclude that the presence of the deck slab cantilever relaxed the two-way action of the barrier wall as a result of the bending deformation in the cantilever.

Another major horizontal flexural crack appeared at the intersection of the two tapered portion of the barrier front side at 225 kN load and then propagated diagonally towards the top of the barrier at the ends of the loaded length at 275 kN. Other horizontal cracks appeared along the loaded length of the barrier on its top tapered portion as depicted in Figure 4.14(f). Then, a sudden and major punching shear crack occurred at the top of the barrier just on the left side of the loaded length as depicted in Figure 4.14(i). At the same time, a local punching shear crack was observed at the top of the barrier wall between the timber blocks in the loading frame as depicted in Figure 4.14(j). However, this local punching crack did not propagate further while trying to increase the applied load using the hydraulic jack. On the other hand, a punching shear crack appeared just at the right side of the loaded length as depicted in Figure 4.14(k). While trying increase the applied load, the barrier wall continued to deform to the extent that the punching shear crack to the left and right of the loaded length propagated toward each other to form a complete punching shear crack at the back of the barrier wall as depicted in Figure 4.14(m). After testing, the barrier wall was saw cut vertically between the two timber blocks used to apply the line loading as well as at the right and left ends of the loaded length. Figure 4.15 depicts the punching shear crack at each location with an average angle of 40°.

The barrier wall eventually failed due to punching shear at a load of 360 kN which is almost the CHBDC design load of 357 kN. Figure 4.16 shows the load-deflection relationship for specimen S-4. At the failure load, the maximum recorded deflection at the loaded end of the barrier was 27 mm, while the maximum deflections at barrier ends were 20 mm and 17 mm, respectively. The recorded barrier uplift at the location of the tie-down system was 4.9 mm at the failure load. The deck slab maximum deflections at its ends were 16 mm and 18 mm at ultimate load, which confirmed to be considerable bending deformation of the deck slab cantilever and associated failure mode. A few horizontal flexural cracks appeared on top of the deck slab cantilever at the location of applied loading at 125 kN and propagated towards the two ends of the specimen with increase in applied load. Some of these cracks reached the ends of the specimen at 200 kN load and then appeared propagating through the cantilever thickness as depicted in Figures 4.14(c) and 4.14(e).

Figure 4.14 (m) shows two major cracks that are almost vertical at the back face of the barrier wall initiated at 275 kN and 325 kN at distances 1 m and 0.75 m from the mid-point of the barrier length, respectively. These two cracks propagated towards the bottom of the barrier wall with increase in applied load. By comparing results of specimen S-3 and S-4, one may observe that the presence of the deck slab cantilever increased the barrier lateral deflection due to bending deformation in the cantilever. Also, the barrier top deflections at the specimen ends in case of the presence of deck slab cantilever are more than those recorded for the barrier supported on the undeformable concrete base. Moreover, the barrier flexural capacity decreased by 14% with the use of the deck slab cantilever.

a) Recording flexural cracks in the deck slab cantilever during testing

b) Punching shear crack appeared at the south end of the timber block of the loading frame

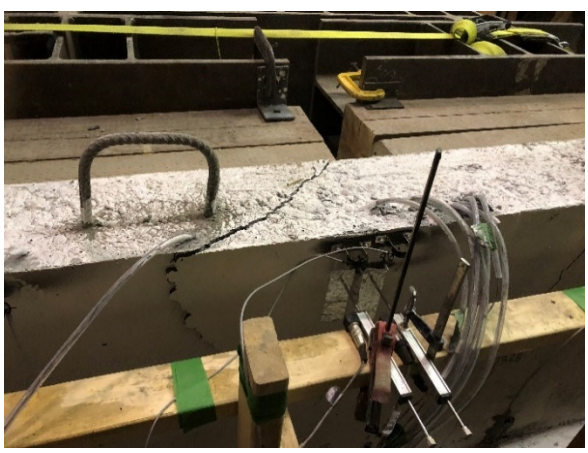

c) Local punching shear crack appeared in the gap between the two timber blocks of loading frame

d) Punching shear crack appeared at the north end of the timber block of the loading frame

Figure 4.13 Views of crack pattern and failure mode for specimen S-4 before removing the testing frame

a) Crack pattern after failure, looking north

b) Crack pattern after failure, looking south

c) Flexural cracks in the cantilever end at south side

d) Flexural cracks in the cantilever end at the north side

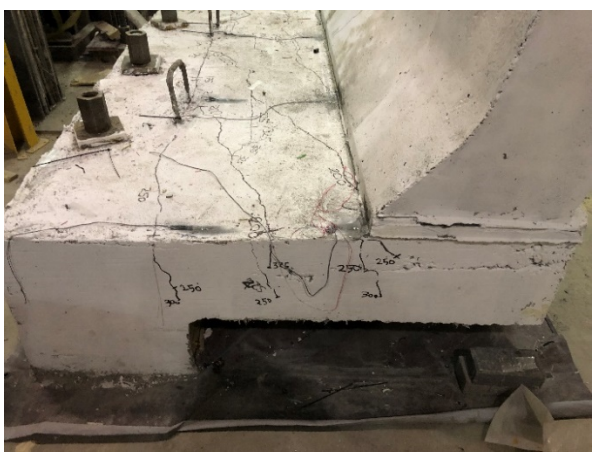

e) Flexural cracks propagated further into cantilever thickness with increase in load the loaded

f) Flexural cracks extending all over the deck cantilever within and outside length

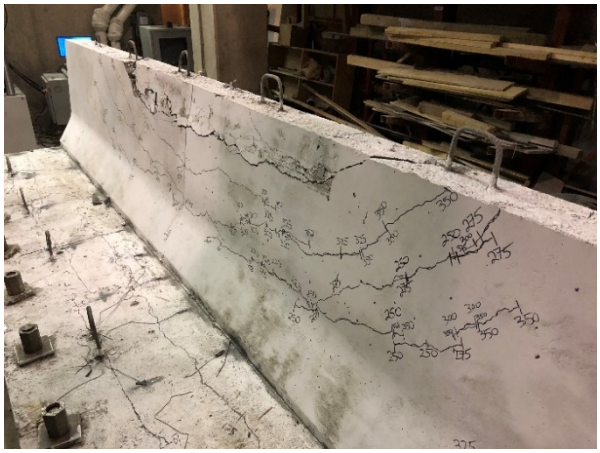

g) Looking south, horizontal cracks within the loaded length, in the tapered portion only, extending diagonally in the unloaded barrier portion

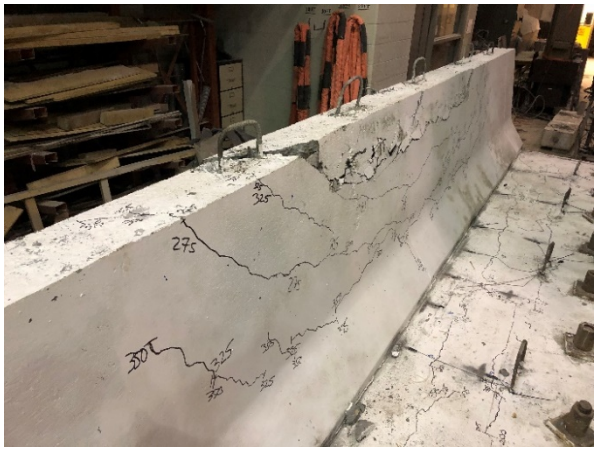

h) Looking north, horizontal cracks within the loaded length, in the tapered portion only, extending diagonally in the unloaded barrier portion

i) First punching shear crack to appear at the south end of the loaded length

j) Local punching shear crack accompanied the first punching shear crack without extending further when attempting to increase the applied load

k) Second punching shear crack appeared at the north end of the loaded length when attempting to increase the applied load

l) Punching shear cracks at beginning and end of the loaded length jointed together with signs of concrete popout when attempting to increase applied load

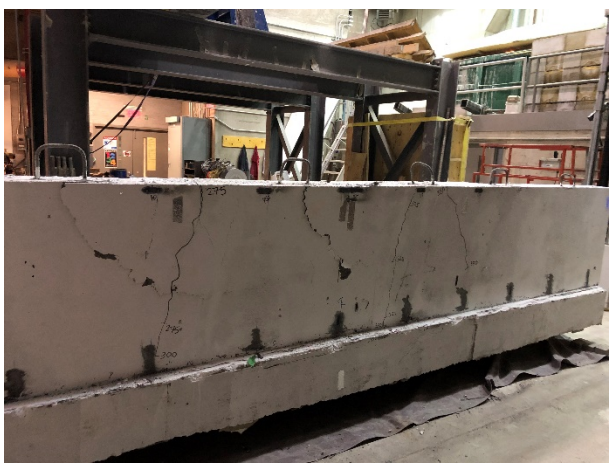

m) Slightly vertical cracks appeared within the loaded length close to failure load

n) Punching shear crack at the south end of the loaded length

Figure 4.14 Views of crack pattern and failure mode for specimen S-4 after removing the testing frame


a) Saw cast at 1 m away from the centre of applied load towards the south end showing punching shear crack


b) Saw cast at 100 mm away from the centre of applied load towards the north end showing 40° angle for the global punching shear crack while the local punching shear crack appeared on top of it in the left photo

c) Saw cast at 1 m away from the centre of applied load towards the south end showing punching a 40° punching shear crack

Figure 4.15 Views of cracks and punching failure mode for specimen S-4 after saw-cut

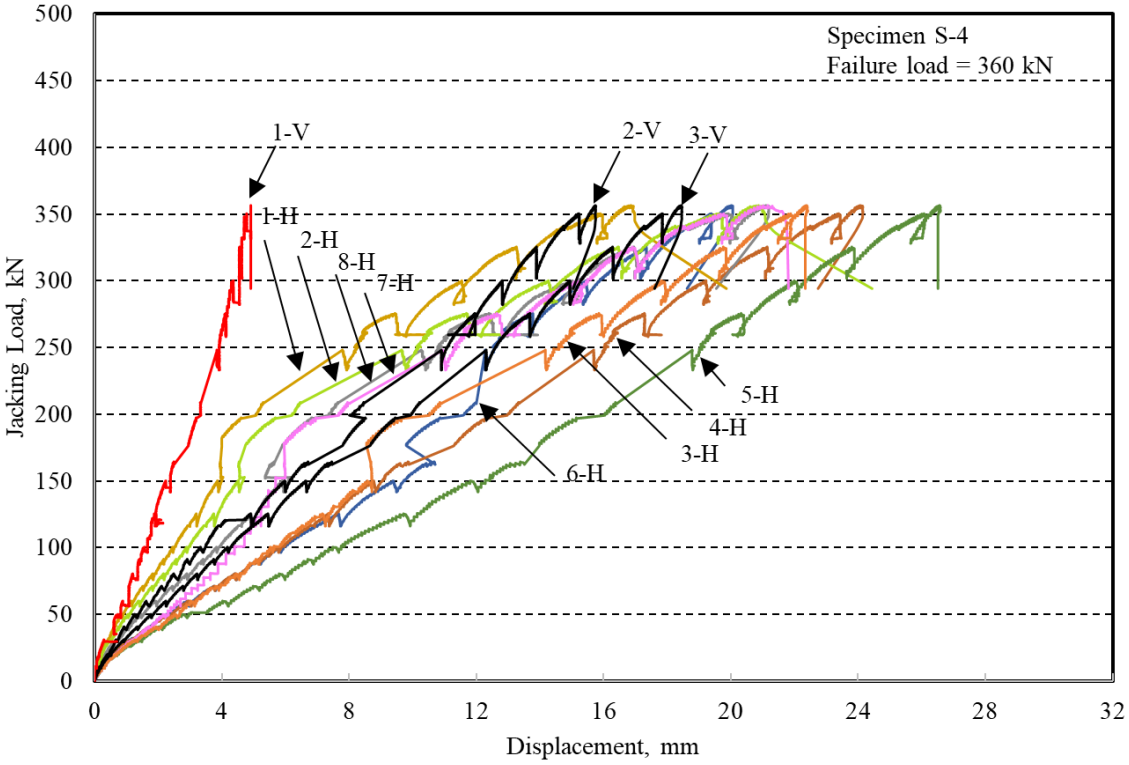

Figure 4.16 Load-deflection relationship for specimen S-4

Chapter V

Conclusions and Recommendations for Future Study

5.1 General

Bridge Design Specifications specify equations for the flexural capacity of concrete barriers subjected to vehicle impact based on the yield-line theory. However, no experimental testing nor computer modelling was found in the literature to support the AASHTO-LRFD triangular yield-line failure pattern. The objective of this study is to generate experimental research data on the behavior of Test-Level 5 (TL-5) concrete barrier reinforced with stainless-steel bars when subjected to transverse vehicular loading. The experimental program included testing four actual-size barriers, two of 6.5 m length and two of 4.5 m length. One barrier in each group was cast over a thick undeformable concrete base, while the other barrier was cast over a short slab cantilever. The 6.5 m long barriers were tested under a transverse line load centered at their mid-length, while the 4.5 m long barriers were tested under exterior line loading.

Experimental results were reported in the form of crack pattern, failure mode, load-deflection relationships and ultimate load carrying capacities. The following sections summarize the conclusions reached in this research and recommendations for future research.

5.2 Conclusions

Based on the experimental findings, the following conclusions were drawn.

1- A trapezoidal flexural crack pattern occurred in the barrier wall which is in contrast to the AASHTO-LRFD triangular yield-line pattern. Also, in contrast to the presence of vertical crack at the back face of the barrier wall in the AASHTO-LRFD yield-line pattern, no vertical crack appeared in the tested barrier walls.

2- The 4.5 m long barrier supported on a thick concrete slab and the two 6.5 m long barriers failed in a punching shear mode. While the 4.5 m long barrier supported on a cantilever, failed due to flexural cracks in the barrier wall and the slab cantilever along with anchorage cracks at the bottom end of the diagonal bent bars in the barrier wall embedded in the deck slab.

3- The experimental transverse capacity of the tested barriers was greater than or equal to the design value in the Canadian Highway Bridge Design Code. However, it is recommended to increase the embedment length of the diagonal bent bars at the barrier-deck junction to be 185 mm instead of 125 mm to assist in avoiding the observed flexural/anchorage failure, leading to a greater applied loading.
4- The barrier casted integrally with a deck slab cantilever exhibited 14% smaller load carrying capacity than that mounted over a nondeformable concrete base. Also, the transverse deformation of the barrier wall mounted over a deck cantilever is more than that for the barrier wall mounted over the nondeformable base, as expected.

5.2 Recommendation for future study

The following recommendations are proposed for future research.

1- Conduct finite-element computer modelling to determine the transverse capacity of different barrier types and determine the range of barrier geometry and reinforcement reach either punching shear failure or the yield-line failure pattern.
2- Conduct experimental and numerical studies on fibre-reinforced concrete (FRC), stainless-steel barriers to optimize the amount of the stainless-steel for market competitiveness with other reinforcement types.

References

American Concrete Institute. (2005). Building Code Requirements for Structural Concrete (ACI 318-05), and Commentary (ACI 318R-05). *ACI 318*, 432.

BS 8110. (1997). Structural Use of Concrete. Part 1; Code of Practice for Design and Construction. *Technical Committee B/525, Building and Civil Engineering Structures*, 238.

Buth, E., Williams, W., Bligh, R., Menges, W., & Haug, R. (2002). *Performance Of The Txdot T202 (Mod) Bridge Rail Reinforced With Fiber Reinforced Polymer Bars.* Austin: Texas Transportation Institute.

CEB-FIP. (1993). Design of Concrete Structures. Comite' Eruo-International du Beton. *CEB-FIP Model Code 1990*, 438.

Charron, J., Niamba, E., Massicotte, B., & . (2011, May). Static and Dynamic Behavior of High- and Ultrahigh-Performance Fiber-Reinforced Concrete Precast Bridge Parapets. *Journal of Bridge Engineering, 16*(3), 413-421.

CSA Group. (2004). Design of Concrete Structures, CSA-A23.3-04. *Canadian Standards Associations*, 240.

CSA Group. (2014). S6-14 Canadian Highway Bridge Design Code. Mississauga.

El-Salakawy, E., & Rubiat Islam, M. (2014, June). Repair of GFRP-Reinforced Concrete Bridge Barriers. *Journal of Bridge Engineering, 19*(6), 04014016-1 - 04014016-11.

Eurocode 2. (2004). Design of Concrete Structures. European Standard. BS-EN 1992-1-1. *General Rules and Rules for Buildings*, 99.

Fadaee, M., Sennah, K., & Khederzadeh, H. R. (2018). Flexural Capacity of Steel-Reinforced Concrete Tl-5 Bridge Barrier Using Modified Trapezoidal Yield-Line Failure Equations. *Canadian Society for Civil Engineering*, (pp. 143-1 - 143-9). Quebec City.

Jacobson, D., Bank, L., Olivia, M., & Russell, J. (2005). Punching Shear Capacity of Double Layer FRP Grid Reinforced Slabs. *ACI Special Publication* (pp. SP - 230-49, pp. 857-875). ACI.

Japanese Society of Civil Engineering (JSCE). (2007). Standard Specifications for Concrete Structures. *JSCE Concrete Committee*, 503.

Khederzadeh, H., & Sennah, K. (2014). *Development of Innovative Designs of Bridge Barrier System Incorporating Reinforcing Steel or GFRP Bars.* Toronto: Hamidreza Khederzadeh.

Lafarge. (2020). *Lafarge - Building better cities*. Retrieved Febuary 21, 2020, from https://www.lafarge.ca/en

Matthys, S., & Taerwe, L. (2000). Concrete Slabs Reinforced with FRP Grids, Part II: Punching Resistance. *ASCE Journal of Composites for Constructions, 4*(3), 154-161.

Rosenbaugh, S. K., Sicking, D. L., & Fakker, R. K. (2007). *Development of a TL-5 Vertical Faced Concrete Median Barrier Incorporating Head Ejection Criteria.* University of Nebraska-Lincoln.

Rostami, M., Sennah, K., Afefy, H. M., & . (2017). Ultimate Capacity of Barrier–Deck Anchorage in MTQ TL-5 Barrier Reinforced with Headed-End, High-Modulus, Sand-Coated GFRP Bars. *NRC Research Press*, 263-278.

Salit Specialty Rebar. (2017). *Salit Specialty Rebar*. Retrieved Febuary 21, 2020, from https://stainlessrebar.com/products/rebar/

Sennah, K., & Hedjazi, S. (2018). Structural Qualification of a Developed GFRP-Reinforced TL-5 Concrete Bridge Barrier Using Vehicle Crash Testing. *International Journal Of Crashworthiness*, 2916-313.